LRP 646/99   October 1999

Papers presented at the
**IAEA Technical Committee Meeting
on ECRH Physics and
Technology for Fusion Devices and EC-11**

Oh-arai, Japan, October 4-8, 1999

LIST OF CONTENTS

European High-Power CW gyrotron development for ECRH systems

S. Alberti[a], A. Arnold[b], E. Borie[b], G. Dammertz[b], V. Erckmann[c], P. Garin[d],
E. Giguet[e], S. Illy[b], G. Le Cloarec[e], Y. Le Goff[e], R. Magne[d], G. Michel[c],
B. Piosczyk[b], C. Tran[e], M.Q. Tran[a], M. Thumm[b], D. Wagner[f]

[a] Centre de Recherche en Physique des Plasmas, Association Euratom–Confédération Suisse,
Ecole Polytechnique Fédérale de Lausanne, CH-1015 Lausanne, Switzerland
[b] Forschungszentrum Karlsruhe, Association Euratom-FZK, IHM/PMW Postfach 3640,
D-76021 Karlsruhe, Germany
[c] Max.Planck-Institut für Plasmaphysik (IPP), Association Euratom, 85748 Garching, Germany
[d] Association Euratom-CEA, Département de Recherches sur la Fusion Contrôlée,
F-13108 Saint Paul Lez Durance, France
[e] Thomson Tubes Electroniques, 2 Rue Latécoère, F-78141 Vélizy-Villacoublay, France
[f] Institut für Plasmaforschung, Universität Stuttgart, Pfaffenwaldring 31, D-70569 Stuttgart

ABSTRACT

The development of high power CW gyrotrons for ECRH heating of fusion relevant plasmas has in progress for several years in a joint collaboration between different European research institutes and an industrial partner. Two development are on going, aiming respectively towards a 0.5MW-210s gyrotron at 118GHz for the tokamaks TCV of CRPP (2s pulse length) and Tore Supra of CEA (210s pulse length), and towards a 1MW-CW gyrotron at 140GHz for the stellarator W7-X under construction in Greifswald.

Series 118GHz gyrotrons have been delivered to CRPP and CEA. Long pulse results (15.5s at 400kW) as well as considerations on power modulation capabilities of the tube and on long pulse effects are discussed.

In a second development program, a 1MW/CW 140 GHz gyrotron with a CVD diamond window and a single-stage depressed collector has been designed and constructed as a first prototype for the 10 MW ECRH system of the new stellarator experiment Wendelstein 7-X of IPP Greifswald/Germany. The gyrotron operates in the $TE_{28,8}$ cavity mode and provides a linearly polarized, $TEM_{0,0}$ Gaussian RF beam. It is composed of a diode MIG gun, an improved beam tunnel, a high-mode purity low-ohmic loss cavity, an optimized non-linear up-taper, a highly efficient internal quasi-optical mode converter employing an improved launcher together with one quasi-elliptical and two beam shaping reflectors, a large single stage depressed collector at ground potential with a beam sweeping magnet, and a horizontal RF output.

I. INTRODUCTION

The use of electron cyclotron (EC) waves on different tokamak and stellarator experiments has in the past years demonstrated the functions of EC waves in fusion relevant plasmas in terms of: plasma breakdown, highly efficient localized heating and current drive [1], MHD control [2]. In addition, EC waves system offer a relative simplicity and versatility of the launcher system of the quasi-optical launcher system.

In parallel to the application of EC waves for fusion plasmas, the development of the gyrotron sources has also made major advances and sources in the range of frequencies between 70 and 170 GHz, at power levels between 0.5 and 1MW and efficiencies in the range between 25 and 50 % are presently available for pulse lengths in excess of several seconds. A major breakthrough for a CW compatible source is the use of a CVD diamond window which allows the design and the operation of a CW tube at the 1MW power level [3]. The single stage depressed collector brings the overall efficiency of the gyrotron in the 50% range and at the same time significantly decreases the thermal loading inside the gyrotron [4]. In the past few years, the main issue was related with the rf pulse length extension at full design parameters.

In this article, we report on a significant pulse length extension increase on the ongoing development of a prototype gyrotron operating at 118GHz/0.5MW with a cryogenic sapphire window. The best performance reached so far has produced an energy per pulse as high as 6.2MJ ($P_{RF} = 400$kW, $T_{RF} = 15.5$s) which is approximately twice as high as previously achieved values in gyrotrons operating at this frequencies and power levels. No intrinsic limitations on further extension have been observed on the gyrotron, the

limitations being so far mainly due to external systems.

The know-how acquired in the development and operation of the 118GHz gyrotron, was used in the frame of a new development of a 1MW/140GHz CW-gyrotron with a CVD diamond window and single-stage depressed collector. The design parameters of the tube and its status are presented.

II. EXPERIMENTAL RESULTS OF 118GHZ/210S GYROTRON FOR TORE SUPRA

For the ECRH program of the tokamaks Tore Supra (Association Euratom-CEA) and TCV (Association Euratom-Confédération Suisse), a 118GHz gyrotron capable of delivering 0.5MW in pulses of 210s was designed and built. A detailed description of the gyrotron was given in references [5-7]. A picture of the 118GHz gyrotron installed in the gyrotron hall of TCV is shown in Fig.1.
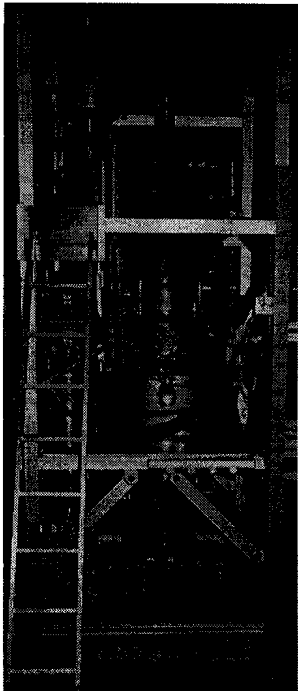

FIG. 1. Picture of the 118GHz gyrotron.

A. Design Parameters

The tube is composed of a triode type electron MIG gun, an improved beam tunnel with an aperiodic dielectric loading structure, a low-ohmic-losses (Glidcop) cavity operating in the $TE_{22,6}$ mode, an optimized non-linear output taper, a high efficient internal quasi-optical converter made of rippled-wall launcher followed by three mirrors [8], a large collector (internal diameter $\phi = 300mm$) making use of an AC sweeping system (7Hz sinusoidal), and a lateral RF output (fundamental $TEM_{0,0}$ gaussian mode) through a liquid nitrogen edge-cooled single-disk sapphire window [9]. Four ion pumps located inside the tube and making use of the superconducting (SC) magnet stray field control the tube vacuum. Table I summarizes the design and operating parameters presently achieved.

TABLE I. Operating and design parameters of the 118GHz/500kW, $TE_{22,6}$ gyrotron

Parameter	Design	Experiment
Accelerating voltage V_b	81kV	81.5kV
Mod-Anode voltage V_a	24.8kV	24.8kV
Beam current I_b	20A	22A
Cathode-cavity distance	350mm	350mm
Cavity magnetic field B_o	4.58T	4.67T
Magnetic compression	24	24
$\langle\alpha\rangle = v_\perp/v_\parallel$	1.5	NA
$\delta\alpha/\langle\alpha\rangle$	1.8%	NA
Operating mode	$TE_{22,6}$	$TE_{22,6}$
Frequency	118GHz	117.77GHz
Cold cavity Q	1710	1602
Self consistent Q	1650	NA
Electronic efficiency	35 %	33%
Window material	Sapphire	Sapphire
waist at window [mm]	$w_0 = 20$	$w_{0x} = 22.6$
		$w_{0y} = 27.3$
Mode purity @ window	98.8%	95.8%
Overall efficiency	30%	28%

B. RF power modulation with a triode MIG gun

For fast RF power modulation different scenarios have been experimentally investigated. To achieve a moderate RF power modulation depth, modulation of either the cathode voltage V_b or the anode voltage V_a can be performed. Typically a $\Delta V_b = \pm 2.5kV$ or $\Delta V_a = \pm 0.75kV$ gives a variation of output power ΔP_{RF} of $\pm 50kW$.

For larger modulation-depth, both V_b and V_a have to be simultaneously modulated as shown in Fig.2 a). A good measure of the generated power in the cavity can be obtained from the steady state frequency reached after thermal stabilization (Fig.2 b)).
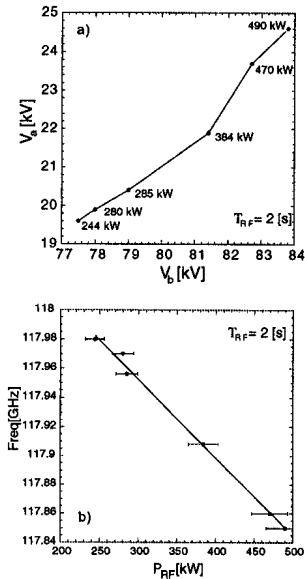
FIG. 2. Fig. a) represents the RF power dependence in the $TE_{22,6}$ mode versus simultaneous change of the beam and anode voltages. Fig. b) shows the thermally-stabilized RF frequency dependence versus RF power. For Fig. b) the power datas are taken from Fig. a) and for the frequencies, the frequency pushing effect due to variation in the beam current ($Freq(I_b)$) is negligible compared to the thermal expansion effect.

The fact that for deep RF power modulation both V_b and V_a need to be modulated, can be understood by observing that at the optimal operating point (close to the boundary between hard and soft excitation regions), the starting current (I_{st}) for the excitation of the $TE_{22,6}$ mode is very close to the operating current I_{opt} as shown in figure 3.
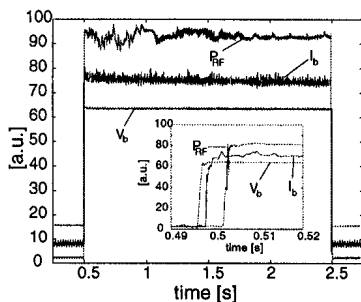

FIG. 3. Time dependence of cathode voltage V_b, beam current I_b and RF power (diode signal) for a 500kW/2s pulse (The different traces have been artificially separated from the zero level for clarity). The anode voltage is not shown. The expanded view shows the startup phase and one observes that the $TE_{22,6}$ cavity mode is excited at a beam current close to the final operating current.

The beam current dependence on V_a, via the Schottky effect, and the pitch angle variation has the consequence that by lowering V_a, the associated electron beam parameters variation eventually brings the operation outside the operation curve for the $TE_{22,6}$ mode. This effect is shown on figure 4 where the efficiency versus magnetic field is calculated with a monomode interaction code for two values of the mod-anode voltage at fixed cathode voltage.
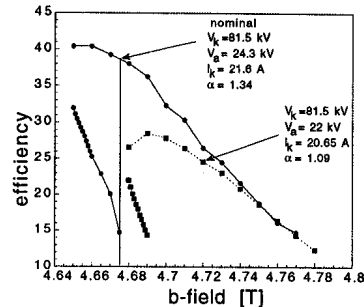

FIG. 4. Mod-anode voltage-modulation effects on the gyrotron operation. Filled circles indicate the operation curve (efficiency versus b-field) at constant current. The vertical continuous line indicates the operational point on this curve in the soft excitation region. The filled square indicate the shift of the nominal operational curve for a lower mod-anode voltage, were the beam parameters variation take into account the Schottky ($dI_b/dV_a = 0.4A/kV$) effect on the beam current and the pitch angle variation.

It is clearly seen that even for a moderate change in V_a, the operation point, within this diagram, can have a significant variation such to reach a non-excitation region. A multimode time-dependent simulation shows that a 100kW decrease in power is obtained by lowering V_a from 24.3kV to 22.8kV and by lowering further V_a below 22.6kV the excitation of the $TE_{22,6}$ mode is lost. The experimental measurements are in excellent agreement with the simulations.

In a diode-gun gyrotron, by modulating the cathode voltage the beam current variation due to the Schottky effect is "compensated" by the variation in the relativistic factor γ in such a way that the detuning variation naturally maintains the operation point in the excitation region.

C. Mode purity at the window

The RF beam characteristics in free space propagation after the sapphire window have been determined by using a phase reconstruction technique [10] based on infrared images taken at four

different distances from the window. Figure 5 shows the result of the amplitude and phase reconstruction at the window position.

reconstructed $|E_{field}|$ profiles @ window
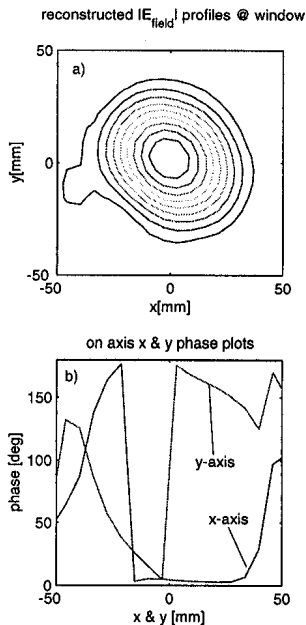
on axis x & y phase plots

FIG. 5. Reconstructed amplitude and phase profiles at the window.

In Fig. 5 a) a E-field contour plot shows that the beam is slightly astigmatic with the ellipse principal axis rotated with respect to the vertical (y-axis) and horizontal (x-axis) axis defined by the gyrotron. In Fig. 5 b), the on-axis phase reconstruction (x and y) are shown and one observes that for the x-axis, the minimum waist w_{0x} is correctly located at the window position. The constant slope on the y-axis phase indicates that the y-axis minimum waist, w_{0y}, is also correctly located at the window but the RF beam is slightly pointing upwards with respect to the window normal. Such a misalignment can be corrected by the mirrors of the matching optics unit (MOU). Simulation using a 3D diffraction theory are in good agreement with the measured profile.

D. Long pulse experiment

The first CRPP series tube has fully passed the onsite acceptance test (P_{RF} = 500kW, Pulse length = 2s) and will be operational on the TCV Tokamak for third harmonic heating in the current of next year. The first CEA series tube has passed the factory acceptance test performed at a pulse length of 5s and is presently being installed

in Cadarache. The factory acceptance test is performed with the MOU connected at the gyrotron and the power is measured in a load connected after a miter bend and 2m of an $HE_{1,1}$ oversized (diameter ϕ = 63.5mm) transmission line. Among other requirements, this acceptance test includes an endurance test consisting in a 3 periods of 8 hours operation at a duty cycle of 1.7%. During these three periods 290 pulses at 500kW/5s were produced with a success rate exceeding 98.5%. A pulse is considered successful when it has not been interrupted by an interlock signal related to the gyrotron operation. The temperature monitoring of different critical parts in the gyrotron (cavity, dimple-wall converter, collector) show that a temperature stabilization is reached within 2s. The internal outgassing of the tube is stabilized after 1s and the ion-pump current (4 pumps operated at 5kV) does not exceed $I_p = 4 - 5\mu A$.

TABLE II. Measured power balance for a 5s RF pulse length @ 500kW measured in the load after the MOU, one miter bend and 2m of $HE_{1,1}$ transmission line. The beam current decrease is due to cathode cooling ($\Delta I_b = -0.9A$ in 5s) and a 3.5% power measurement accuracy is considered.

Parameter	Value
Accelerating voltage V_b	81kV
Beam current I_b (average over 5s)	18.9A
Beam power P_{beam}	1530kW
Power in the load P_{RF}	490kW
Power in beam tunnel P_{bt}	3kW
Power in cavity-launcher P_{cl}	62kW
Power in collector P_{col}	930kW
Power in MOU+$HE_{1,1}$line P_{other}	20kW
Power balance $P_{tot} = \sum P_i$	1505kW ±50kW

The failed pulses during the endurance test were always stopped by the ion-pump current interlock ($I_p > 20\mu A$) with no evidence of arcing observed on the beam current trace. After a failed pulse no conditioning was needed to reobtain a 5s pulse. For a 5s pulse the measured gyrotron power balance is given in table II.

1. Pulse extension beyond 5s on the prototype gyrotron

The prototype gyrotron has passed a factory acceptance test at 5s at the nominal parameters, and the pulse length extension beyond 5s has been performed at CEA-Cadarache with a high voltage power supply compatible with a CW operation. Due to a magnetic field misalignment during the

firsts tests, the cavity and internal converter section of this prototype gyrotron were slightly damaged and subsequently did not allow to reach the nominal rf power level of 500kW. After realigning the magnetic field, a maximum power level of 400kW could be reached, but, compared to the factory acceptance test, a 80% increase in the cavity-launcher power losses was observed. In spite of this abnormal behavior, using a prototype CW evacuated load, the pulse length was extended from 5s to 15.5s within 5 days. The total energy in the RF pulse of 6.2MJ is, at present the highest value presently achieved worldwide for gyrotrons operating at these frequencies and power levels.
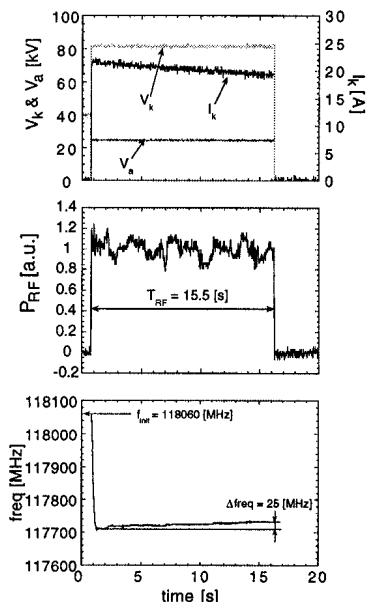

FIG. 6. Longest pulse-length presently achieved with the 118GHz gyrotron. Fig. a) shows the time evolution of V_b, V_a and I_b. An important beam current decrease due to cathode cooling is observed ($\Delta I_b = -2.2A$). Fig. b) shows the RF power trace measured with a diode mounted on a miter bend placed on the $HE_{1,1}$ transmission line after 4m of waveguide. Fig. c) shows the frequency evolution during the pulse and the slight frequency increase after thermal stabilization is associated with a RF power decrease caused by the cathode cooling.

Figure 6 shows the typical time evolution of the relevant parameters for a RF pulse length of 15.5s and power level at the window of 400kW. The current decrease observed on figure 6 a) is due to cathode cooling and is at present one of the limiting factors for further pulse length extension since no power boosting system on the cathode heater power supply is implemented yet. A second limiting factor for the pulse length extension is the

additional outgassing inside the tube due to the damaged cavity-launcher system and also by the important reflection coefficient (Power reflection > 20%) of the evacuated load. Several pulses have been obtained in the 15s range and were always terminated by the the internal ion-pump current interlock. On figure 6 c) one observes that the RF frequency is well stabilized after 1s and the slight increase ($\Delta freq = 25MHz$) is due to the slight power decrease associated to the beam current decrease. The thermally stabilized frequency of $f_{on-site} = 117,720MHz$ for a RF power of 400kW is significantly lower than the value obtained for the same gyrotron ($f_{factory} = 117,780MHz$) during the factory acceptance test at 5s and 500kW. This difference is to be associated with the increased losses in the damaged cavity launcher system.

The implementation of the cathode heater boosting and a modification of the load are currently underway an will allow to further extend the pulse length beyond 15.5s. This extension will be performed on the first series tube for Tore Supra which has already passed the factory acceptance test at 5s.

III. DESIGN OF THE 140GHZ/CW GYROTRON FOR WENDELSTEIN 7-X

A. Magnet and diode MIG gun

As shown in figure 7 the superconducting (SC) magnet configuration is composed of two main coils generating a constant magnetic field B_0 in the interaction region and, for minimizing the cathode-cavity distance, a third SC magnet generating a reverse field allows the control of the magnetic field at the cathode position.
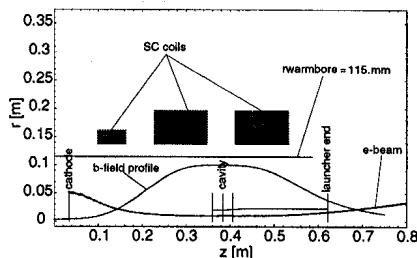

FIG. 7. Coil geometry and electron beam trajectory between cathode and dimple-wall converter output. The cathode and cavity magnetic field can be controlled independently.

The ratio between the cavity field and cathode field B_c is $B_0/B_c = 23.5$. The independent control of the cavity and cathode fields is possible by using two power supplies.

The temperature limited diode MIG electron gun, operates at voltages up to $V_b = 82\text{kV}$ and currents up to $I_b = 42\text{A}$. At this current value, the cathode current density is $j_c = 2.5A/cm^2$. At the nominal operating parameters of $V_b = 81\text{kV}$ and $I_b = 40\text{A}$, the beam properties in the interaction region, calculated with the equilibrium codes DAPHNE [11] and BFCRAY [12], are in good agreement and for an average pitch angle $\langle \alpha \rangle = 1.5$, a RMS pitch angle spread of $\delta\alpha/\langle\alpha\rangle = 1.2\%$ is obtained. The energy spread induced by electrostatic instabilities between the cathode and the cavity was calculated with a time-dependent 2D code, G2DRZ [13]. For minimizing the energy spread, the cathode cavity distance has been minimized: for a cathode cavity center distance of 350mm an RMS energy spread $\delta\gamma/(\langle\gamma\rangle - 1) = 1.7\%$ is calculated.

For fast RF power modulation between 1MW and 0.3MW, the beam accelerating voltage is modulated between $V_b = 81\text{kV}$ and $V_b = 71\text{kV}$. The variation of the pitch angle spread $\delta\alpha/\langle\alpha\rangle$ versus V_b within this range is small. The beam current variation between the two limits of V_b due to the Schottky effect is $\Delta I_b = 2.5 - 3A$. Within these beam properties variations, the diode configuration allows the required deep power modulation by varying the acceleration voltage only.

For suppressing spurious oscillation in the beam tunnel between the gun and the interaction region, an aperiodic loading structure composed by a stack of copper rings and dielectric rings (AlNSiC) has been implemented [14].

B. Cavity

The RF cavity is designed to operate in the $\text{TE}_{28,8}$ with a diffractive quality factor Q_{diff} in the cold cavity approximation $Q_{diff-c} = 855$ and a self-consistent quality factor of $Q_{diff-sc} \simeq 1100$ at the nominal parameters. Mode conversion is reduced by use of angle roundings and of a non-linear uptaper. The resulting mode purity is calculated to be 99.9 % instead of 98.5 % with no roundings and a linear uptaper.

The cavity material is Glidcop and at the nominal parameters, the peak wall losses are below $2\text{kW}/cm^2$, where, for the Glidcop conductivity, the wall temperature ($T_{peak} = 270^{\circ}C$), surface roughness and frequency effects have been taken into account.

Long-pulse effects such as space charge neutralization and cavity thermal expansion have been considered. For a base pressure of $p_0 = 10^{-8}\text{mbar}$, the time scale for complete space charge neutralization is of the order of $\tau_{SC} = 100\text{ms}$ whereas the time scale for radial thermal expansion of the cavity is of the order of $\tau_{therm} = 400 - 500\text{ms}$ if a heat exchange factor $h = 6.2~10^4\text{W}/m^2\text{K}$ is considered.
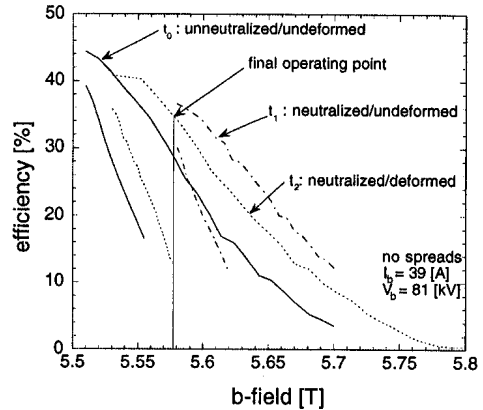

FIG. 8. Monomode calculations of efficiency versus magnetic field at constant current taking into account the long-pulse dynamics of the interaction due to space charge neutralization and cavity wall deformation.

At the nominal beam parameters, and, using a monomode-mode model, the efficiency versus magnetic field curve is shown in figure 8 for the three situations: unneutralized/undeformed (t_0), neutralized/undeformed (t_1) and neutralized/deformed (t_2) where "deformed" means the actual deformed cavity profile calculated at the equilibrium temperature (peak cavity temperature $T_{peak} = 270^{\circ}C$) with a thermomechanical code. The evolution time-scale $t_0 \rightarrow t_1 \rightarrow t_2$ is given above and in fig. 8 the two effects of space-charge neutralization and deformation are shown as if they would occur independently, but in reality they are evolving simultaneously. One notices that depending on the choice of magnetic field value B_0, the RF oscillation can be lost between t_0 and t_1. The selected operating point is chosen such as to remain in the soft excitation region when the system is thermally stabilized (curve t_2). In order to reach an operating frequency of 139.8GHz, the undeformed cavity resonant frequency is designed to be at 140.2GHz.

As shown in Fig. 9, multi-mode simulations taking into account the space-charge neutralization effects show that single mode operation can be achieved with the diode startup. This figure shows

the evolution of the power in various modes during space-charge neutralization, assuming that the $TE_{28,8}$ mode has started to oscillate (the result of a previous simulation). Also note that the time scale on the figure is an artifact of the simulation, and really corresponds to about 100ms.
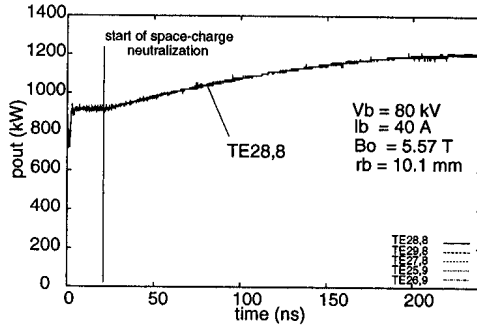

FIG. 9. Output power as a function of time during space charge neutralization. The beam energy increases from 75keV to 80keV, while α decreases from 1.42 to 1.29.

C. Quasi-optical converter

The RF beam is separated from the electron beam by means of an optimized quasi-optical mode converter consisting of a rippled-wall waveguide launcher followed by a mirror of quasi-elliptical shape and two toroidal focusing mirrors which match the beam to the window size (RF beam radius of 23.3mm). The beam waist ($w_0 = 22$mm) lies 250mm after the window. Coupled mode theory [15,16] is used in the design and analysis of the launcher, and the reflectors are designed with Gaussian optics and diffraction theory. The launcher shape has an improved perturbation structure leading to optimum phasing and suppression of spurious oscillations. The distance from the electron beam to the launcher wall is always larger than 3.5-4mm. The total calculated ohmic losses in the launcher and on the three mirrors are around 3.2%, whereas the theoretical diffraction losses are only 1.1%. Figure 10 shows a contour plot of the ohmic losses power density inside the rippled-wall waveguide as well as an H-field contour plot at the radiating aperture. To verify the proper behavior of the device, a cold test setup has been built.
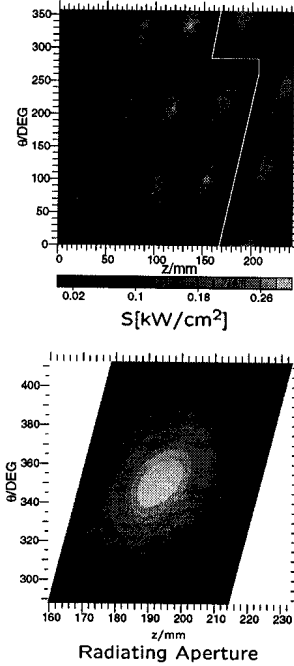

FIG. 10. Top figure: contour plot of ohmic losses power density inside the rippled-wall converter. The angular coordinates represents an unrolled cylinder and the axial coordinate is along the cylinder axis. The white line corresponds to the actual physical cut allowing the radiation of the quasi-optical rf beam. Bottom figure: H-field contour plot on the radiating aperture.

D. CVD Diamond window

The output vacuum window unit uses a single, edge-cooled CVD-diamond disk with an outer diameter of 106 mm, a thickness of 1.8mm ($4\lambda/2$) and a window aperture of 88mm. Thermal computations show that for a power of 1MW at 140GHz, a loss tangent of $\tan\delta = 4.10^{-5}$, a permittivity $\epsilon_r = 5.67$, a thermal conductivity of $1900(T/293)^{-1.4}$W/mK (T being the diamond temperature), a cooling rim of 5mm and a heat transfer coefficient of 12kW/m^{2}K to the cooling water at 293K the temperature rise in the center and at the edge will be 61K and 15K, respectively. The absorbed power is 705W and the window temperature stabilization time is of the order of 5s. Due to the brazing material used (Aluminum based) in the window assembly and the Inconel tubes on the window faces, the gyrotron baking temperature was limited to 445°C.

FIG. 11. Picture of the gyrotron CVD diamond window assembly.

In figure 11, a picture of the diamond window assembly installed on the gyrotron is shown.
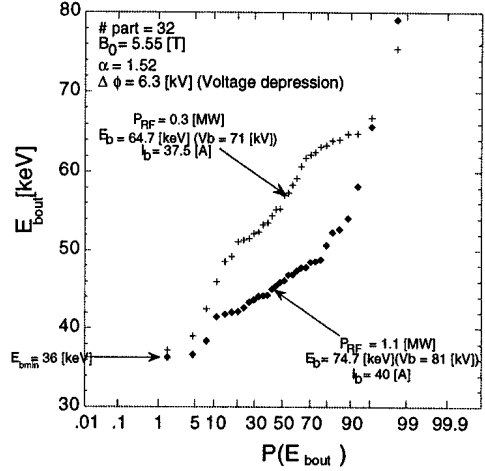

FIG. 12. Electron beam energy distribution function at the cavity output for 1.1MW (filled diamonds) and 0.3MW (crosses) of RF power. The quantity P_{Ebout} is given by $P(Ebout) = \int_0^{Ebout} f(E)dE / \int_0^\infty f(E)dE$ and $f(E)$ is the energy distribution function. The RF power modulation is performed by varying the beam energy only. The current variation induced by the Schottky effect is taken into account.

E. Depressed collector

The diameter and length of the single stage depressed collector are 450mm and 1300mm, respectively. The collector body together with the internal mirror box, the last mirror of the mirror box and the window unit are at ground potential. At a depression voltage of $V_{dep} = 30\text{kV}$, the cathode voltage is set at $V_{cat} = -50\text{kV}$ and the cavity at +30kV. The collector employs DC and AC (10Hz sinusoidal) axial magnetic fields for beam sweeping.

The maximum peak temperature increase on the collector surface has been calculated to be 275°C for 1MW output power. An overall efficiency of $\eta_{tot} = 47\%$ at a retarding voltage of 26kV is calculated. As shown in figure 12 (diamond symbol) the minimum electron kinetic energy at the cavity output is approximately 36keV. The depression voltage acts only on the parallel electron kinetic energy and, since the electron deceleration occurs in a region were the pitch angle $\alpha = 0.3 - 0.4$ is not negligible and the space charge voltage depression $\Delta\Phi_{max} = 8\text{kV}$ is important, the maximum depressed collector voltage cannot exceed 27-28kV.

Fast RF power modulation can be achieved by modulating the beam energy. With a depressed collector system this modulation could be performed either by modulating the cathode voltage or the depressed voltage. However, as shown in figure 12 (crosses) the minimum kinetic energy of the spent beam is independent of the generated RF power level which implies that for minimizing the collector wall thermal loading, only a modulation of the cathode voltage is possible. For a reduced RF power level of 0.3MW the maximum collector temperature is 350°C.

F. High-Power Experiment

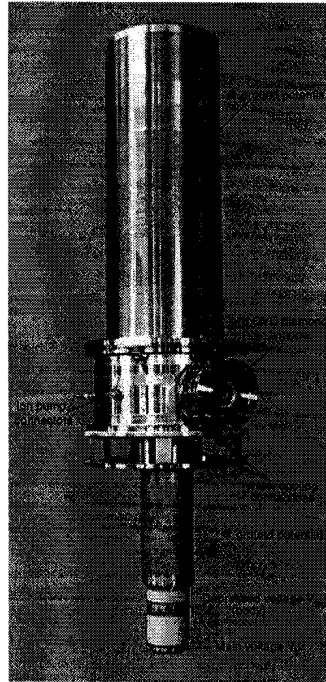A preliminary prototype ("maquette") designed to withstand all the CW constraints is shown in figure 13.

FIG. 13. Picture of the 140GHz gyrotron.

TABLE III. Design parameters of the 140GHz/1MW, $TE_{28,8}$ gyrotron

Parameter	Value
Accelerating voltage V_b	81kV
Beam current I_b	40A
Cathode-cavity distance	350mm
Cavity magnetic field B_o	5.56T
Magnetic compression	23.5
Average pitch angle $\langle \alpha \rangle$	1.5
Space charge depression	5.7kV
Operating mode	$TE_{28,8}$
Frequency (temperature stabilized)	139.8GHz
Cold cavity quality factor	855
Self consistent quality factor	1100
Peak cavity wall loading $\rho_{\Omega peak}$	2kW/cm^2
RF power (cavity)	1.130 MW
Electronic efficiency	35 %
Window material	CVD Diamond
Beam radius @ window	$w = 23.3$mm
Mode purity @ window	98.8%
Voltage depression V_{dep}	27kV
Overall efficiency	48%

The main design parameters are listed in table III. The first tests will begin in November 1999 and performed on a test stand located at FZK.

IV. CONCLUSION

The 118GHz gyrotron development program has demonstrated that the gyrotron physics in a CW regime as well as the technology used are well mastered and successful.

Based on the experience and design philosophy of the 118GHz program, the design and realization of a first prototype 140GHz gyrotron has been achieved and first tests will be started at the end of this year. The 1MW output power in $TE_{28,8}$ mode with a CVD diamond window and a depressed collector makes this design to be compatible with the needs presently considered for ITER where the only difference resides in the frequency of 170GHz needed for ITER.

Within the European gyrotron development program, the technology used in the present ongoing programs will possibly be implemented for fabricating and testing of larger power CW gyrotrons. In this view, the presently ongoing development program at FZK devoted to the study, in medium pulse-length regime, of multimegawatt coaxial-cavity gyrotrons could possibly lead to the design of a 2MW CW coaxial-cavity gyrotron with depressed collector for ITER.

[1] V. Erckmann, and U. Gasparino, Electron cyclotron resonance heating and current drive in toroidal fusion plasmas, Plasma Phys. Control. Fusion 36, 1869 (1994).

[2] H. Zohm, et al., Experiments on neoclassical tearing mode stabilization by ECCD in ASDEX Upgrade., Nucl. Fusion 39, 577 (1999).

[3] K. Sakamoto, A. Kasugai, M. Tsuneoka, K. Takashi, T. Imai, T. Kariya, and Y. Mitsunaka, High power 170GHz gyrotron with synthetic diamond window, Rev. Sci. Instrum. 70, 208 (1999).

[4] V.E. Zapevalov et al., Development of 1MW output power level gyrotron for ITER, in *Proceedings of 22nd International Conference on Infrared and Millimeter Waves, Wintergreen, USA, 1997*, edited by P. Freund.

[5] E. Giguet, C. Tran, P. Thouvenin, P. Garin, M. Pain, S. Alberti, M.Q. Tran, and M. Thumm, Operation of a 118GHz-0.5MW gyrotron with cryogenic window, in *Proceedings of 20th International Conference on Infrared and Millimeter Waves, Orlando, USA, 1995*, edited by R.J. Temkin.

[6] S. Alberti, O. Braz, P. Garin, E. Giguet, M. Pain, P. Thouvenin, M. Thumm, C. Tran, M.Q. Tran, Long pulse operation of a 0.5MW-118GHz gyrotron with cryogenic window, in *Proceedings of 21st International Conference on Infrared and Millimeter Waves, Berlin, Germany, 1996*, edited by M. von Ortenberg and H.U. Mueller.

[7] C. Tran, E. Giguet, P. Thouvenin, P. Garin, M. Pain, S. Alberti, M.Q. Tran, and M. Thumm,

Status of the 118GHz-0.5MW quasi-CW gyrotron for Tore Supra and TCV Tokamaks, in *Proceedings of 23rd International Conference on Infrared and Millimeter Waves, Colchester, UK, 1998*, edited by T.J. Parker and S.R.P. Smith, ISBN 0 9533839 0 3.

[8] O. Braz, M. Losert, A. Mobius, M. Thumm, R. Curdroy, E. Giguet,C. Tran, M.Q. Tran, and D.R. Whaley, Cold tests and high power measurements on an advanced quasi-optical mode converter for a 118GHz gyrotron, in *Proceedings of 20th International Conference on Infrared and Millimeter Waves, Orlando, USA, 1995*, edited by R.J. Temkin.

[9] P. Garin, G. Bon-Mardion, M. Pain, R. Heidinger, M. Thumm, A. Dubrovin, E. Giguet, C. Tran, Cryogenically cooled window: a new step toward CW gyrotron operation, in *Proceedings of 20th International Conference on Infrared and Millimeter Waves, Orlando, USA, 1995*, edited by R.J. Temkin.

[10] A.V. Chirkov, G.G. Denisov, N.L. Aleksandrov, 3D wavebeam field reconstruction from intensity measurements in a few cross sections, Optics Communications **115**, 449 (1995).

[11] T.M. Tran, D.R. Whaley, R. Gruber, and S. Merazzi, DAPHNE, a 2D axisymmetric Electron Gun Simulation Code, in *Proceedings of the 6th Joint EPS-APS International Conference on Physics Computing* (European Physical Society, Petit-Lancy, Switzerland 1994), p.492.

[12] E. Borie, C. Grüber, T. Westermann, Calculation of MIG guns for gyrotrons using the BFCPIC code, Int. J. Electronics **78**, 789 (1995).

[13] T.M. Tran, G. Jost, K. Appert, S. Alberti, M. Pedrozzi, Particle-in-cell (PIC) simulations of beam instabilities in gyrotrons, Phys. Plasmas **4**, 3043 (1997).

[14] M. Pedrozzi, S. Alberti, J.P. Hogge, M.Q. Tran, and T.M. Tran, Electron beam instabilities in gyrotron beam tunnels, Phys. Plasmas **5**, 2421 (1998).

[15] A.V. Gaponov-Grekhov, and M.I. Petelin, High-power high-frequency classical electronics: status, trends and problems, Proc. Int. Workshop on Strong Microwaves in Plasmas (Suzdal), IAP ed., 677-692 (1991).

[16] A. Moebius, and M. Thumm, *Gyrotron Oscillators* (Taylor and Francis, London), Edited by C. J. Edgcombe, ISBN 0 7484 0019 2, Chap. 7.

Sustained Fully Non-Inductive Scenarios Using Pressure and Current Profile Control with ECCD

O. Sauter, T.P. Goodman, S. Coda, M. Henderson, F. Hofmann, J.-P. Hogge, Y. Peysson[a)],
Z.A. Pietrzyk, R. Pitts, H. Reimerdes, H. Weisen

Centre de Recherches en Physique des Plasmas, Ecole Polytechnique Fédérale de Lausanne,
Association EURATOM - Confédération Suisse, CH-1015 Lausanne, Switzerland
[a)]CEA/Cadarache, Association EURATOM-CEA, France

Abstract

The ECW system on TCV allows the study of a wide range of poloidal and toroidal launch angles. Both ECH and ECCD experiments have been performed to demonstrate the modification of the electron temperature and current profiles. In particular a multi-channel hard X-ray camera (on loan from Cadarache) clearly shows the generation of a high energy electron tail which increases with increasing toroidal launch angle. Using a scenario with three 0.5MW gyrotrons providing on-axis CO-CD, we have obtained full current replacement of 150kA. However, this leads to very peaked profiles which are MHD unstable and the discharge disrupts. By careful distribution of the power deposition and current source profiles over the minor radius, we have obtained steady-state scenarios up to 124kA with $T_{e0} \approx 3.5$keV and $\bar{n}_e = 10^{19}$m^{-3}. These scenarios are sustained for 1.9s, that is, more than 900 confinement times and more than 10 current redistribution times. Therefore, both the pressure and current profiles are sustained by the 1.5MW of ECCD power. By lowering the feedback plasma current demand, the ohmic transformer is recharged; this provides a very good diagnostic of the total non-inductive current driven in these scenarios.

1. Introduction

The Tokamak à Configuration Variable (TCV) [1] has major radius R=0.9 m, minor radius a=0.24 m and vacuum vessel elongation κ=3. These characteristics allow the creation of a wide variety of plasma shapes, including 1) low to moderate κ (1-1.5) plasmas which can be displaced vertically by ±0.4m, and 2) high κ (2-3, 2.58 achieved) plasmas. In particular the confinement properties of plasmas of elongation 1< κ < 2.1 and triangularity -0.5 < δ <0.5 have been documented in a recent study [2]. The electron cyclotron heating (ECH) and current drive (ECCD or CD) system of TCV has been designed to take full advantage of this flexibility in plasma configuration.

The EC system [3] is based on clusters of three 0.5 MW, 2.0 s gyrotrons. Each cluster is powered by a regulated high voltage power supply. The completed installation will consist of two clusters at 82.7 GHz (2nd harmonic electron cyclotron resonance) and one at 118 GHz (3rd harmonic electron cyclotron resonance) for a total of 4.5 MW. For the experiments reported here, one 82.7 GHz cluster was used. The second cluster (82.7 GHz) will be available in autumn 1999 and the third cluster (118 GHz) in 2000.

All gyrotrons are connected to TCV via individual matching optics units (MOU's) and evacuated 63.5 mm diameter corrugated waveguides. The polarization of each beam is set by a polarizer located in the MOU and can be changed from shot to shot. In addition, the gyrotron output can be switched from TCV to a calorimetric load for power measurements or to allow different combinations of gyrotrons to be used, depending on the needs of a particular experiment.

Of particular importance is the flexibility of the launching antennas (launchers) and the coverage of the plasma that they provide. Each of the 82.7 GHz gyrotrons is connected to a separate launcher which is capable of sweeping the microwave beam through 48° in a plane in ~300 ms. The sweep plane can be rotated ±180° about the torus major radius between shots but is fixed

during a shot. For example, at $0°$ the beam points downwards and lies in the poloidal plane of the torus, at $\pm 180°$ the beam points upwards and at $\pm 90°$ the beam lies in a horizontal plane providing co- or counter- current drive (CO-CD or CNT-CD). In the latter case, the sweep of the beam provides a variation of the toroidal injection angle during one shot. At intermediate rotation angles, the usual (projected) poloidal and toroidal injection angles in the tokamak frame-of-reference are coupled in the launcher frame such that both will vary during a sweep of the beam.

Sweeping of the beam has proved important for investigations of MHD stability [4]; however, for steady-state experiments this feature is not needed or desired. Nevertheless, the ability to aim the beams precisely is required and the sweeps have allowed the confirmation of the designed precision ($\pm 0.2°$ in plane, $\pm 0.8°$ in rotation), in situ [5]. The possibility of aiming the beams separately has been vital to the success of the steady-state ECCD current replacement experiments which we now discuss.

2. Current Drive Efficiency

The linear current drive efficiency is given by $\eta \propto I_{CD}/P \propto T_e/R_0 \; n_e \; (Z_{eff}+5)$, where I_{CD} is the driven or non-inductive current, P the ECCD power, T_e the electron temperature, R_0 the major radius, n_e the local or line-averaged electron density, and Z_{eff} the effective charge of the plasma [6]. Thus, we expect to drive the greatest current non-inductively when aiming near the hot plasma center; in addition n_e and Z_{eff} may also peak centrally to a lesser degree. At the low densities used in the present experiments, Z_{eff} is not directly measurable on TCV, but it is estimated by comparing the Thomson scattering and X-ray emission measurements: its estimated value is $Z_{eff} \approx 5.4$ and is approximately constant or increases very slowly during a 2.0 s discharge. The TCV vacuum vessel has near complete (~90%) coverage with carbon tiles [7] and is regularly boronized. Such high Z_{eff} values imply a high concentration of carbon impurity. However, the total radiated power measured by bolometry is typically less than 15% of the total input power, which is consistent with the high carbon concentration only if the charge state at the edge is already high. Therefore, although profiles of Z_{eff} are not available, they are assumed to be flat. Since the density profiles are also relatively flat, the current drive efficiency is expected to be essentially a function of temperature and line-averaged density for all deposition locations.

Non-inductively driven current arises essentially from a distortion of the maxwellian electron distribution function in velocity space. High energy electrons in the tail of the velocity distribution retain the anisotropy created by the perpendicular acceleration of the electrons. The Doppler term of the single particle resonance condition ($\omega = 2\Omega/\gamma + k_{//}v_{//}$) ensures that particles of high parallel speed will be the first to fall into resonance with the beam along its propagation path. Therefore, the direction of the driven current will depend on the launcher location, which in these experiments is on the low field side (LFS), and on the toroidal angle of injection ($k_{//}$). However, in toroidal devices, at large enough toroidal angles refraction can become a problem and the beam single-pass absorption is incomplete, leading to a decrease of the current driven. The combination of these effects determines the optimum angle of toroidal injection for maximum current drive efficiency, all else being equal.

3. Scan of the toroidal injection angle and measure of high energy tail electrons

A measure of the relative efficiency of the current driven is the temperature of the high energy tail electrons as diagnosed using a hard X-ray camera on loan from the CEA/ Cadarache [8] and adapted to the TCV experimental setup [9]. The chords set-up is shown in Fig. 1. The hard X-ray energy spectra are fitted by exponentials to provide a photon temperature for the fast electrons. As seen on Fig. 2, the photon temperature is much higher for CO- or CNT-CD than for ECH. The ECH temperature measured in this way agrees well with that measured by Thomson scattering [9] and is consistent with a Maxwelllian distribution, whereas a high energy tail is clearly visible during both CO- and CNT-CD. Note that the camera cannot differentiate between the $+v_{//}$ and $-v_{//}$ parts of the distribution function responsible for the bremsstrahlung emission. The lowest energy channels of the ECCD cases are not used in the

temperature fitting since they are still affected by the thermal bulk radiation. These results suggest that TORAY ray tracing calculations may underestimate the driven current and miscalculate the ray paths as they do not take into account the suprathermal tail.

To determine the angle of maximum current drive efficiency, the toroidal angle of injection was varied over a series of discharges. The angle was varied from -35° to $+35^\circ$ in steps of 7°. The polarization was optimized for each step according to a zero density approximation of the cold dispersion relation in order to maintain injection in the quasi-X-mode [10]. The photon counts emitted from the plasma center in the range 40-50keV are shown as a function of the toroidal launching angle in Fig. 3. One sees in particular that the value keeps increasing up to the maximum "CO" angle, namely 35°. Although larger toroidal angles can be explored, set-up of the experiment and interpretation of the results is then complicated by beam refraction. Therefore, we have used 35° thus far for the demonstration of full current replacement discussed later in the paper.

We also show in Fig. 4 the loop voltage at the plasma surface, normlized by $T_{e0}^{-3/2}$, namely by the temperature dependence of the resistivity: this normalized quatity is roughly proportional to the non-inductive current, if the profiles are similar, i.e. $V_s T_{e0}^{3/2} \propto I_p - I_{CD} - I_{BS}$, where I_p is fixed (173kA) and I_{BS} is the bootstrap current ($\approx 10\%$). Therefore, everything else being about constant, changing only the toroidal angle should only modify I_{CD}: in particular, CO-CD should decrease $V_s T_{e0}^{3/2}$, while CNT-CD should increase it as compared to the ECH case. This is confirmed by the experimental results, as seen in Fig. 4. The dependence is linear on the CO-CD side. In some of the CNT-CD cases, improved confinement is obtained leading to very high (though transient) central temperatures. The drastically different plasma conditions in these cases may account for the departure from linearity. These results show that 35°-40° is the optimum angle for CO-CD, in the range studied. We also confirm that comparing CO- and CNT-CD cases to measure the amount of driven current is not justified in most cases, as already shown by previous tokamak experiments. However, a direct comparison between the ECH and CO-CD cases at different angles is justified by the similarity in plasma conditions. This also confirms that the heating effect of the EC waves in the CO-CD case is comparable to that in the ECH case, the bootstrap current is therefore of similar magnitude in the two cases.

4. CO-CD with Central Deposition

In order to obtain the maximum driven current, we aimed all the gyrotrons toward the plasma center, as sketched in Fig. 5a. We see in Fig. 5b that the loop voltage quickly drops to zero for a plasma current of 153kA and a central density of $1.75 \ 10^{19} m^{-3}$, yielding a current drive efficiency of $\eta_{20} = n_{e20} R I_{CD}/P = 0.016$. However, MHD activity is steadily increasing as the plasma pressure and current profiles re-adjust to the new source of current. The steady state is not reached as the discharge ends in a distruption about 150ms after the start of ECCD. This configuration was repeated several times, each pulse ending in a disruption. Thomson scattering measurements show a peaking of the electron pressure, and the internal inductance as determined by the LIUQE reconstruction code increases. Thus all indications are that the profiles become too peaked and lead to instability. Steady state full current replacement has not been possible with only central power deposition. Note that even if this scheme had been successful, it would have led to a plasma with pressure and current concentrated in the central part, resulting in an effective plasma minor radius decreased by about a factor of two.

5. Steady-State CO-CD: Distributed Deposition

With the goal of full replacement of the Ohmic current under steady-state conditions, a loss of current drive efficiency has to be accepted and the beams are distributed to better sustain broad pressure and current profiles. Initially the beams were distributed at normalized radii of $\rho \approx 0$, 0.25 and 0.55 (ρ here is defined as the normalized square-root of the toroidal magnetic flux). These pulses ended in disruptions as the profiles were still too peaked. Finally, the distribution was set at $\rho \approx 0$, 0.35 and 0.55, as shown in Fig. 6. The power deposition and driven current profiles are also shown as calculated by Toray. The time traces for the full current replacement scenario, shot 16099, are shown in Fig. 7. It can clearly be seen that the current in the ohmic

transformer (I_{OH}) changes very rapidly and is flat for 1.9s, providing unambiguous evidence that no inductive current is driven in the plasma. Accordingly, the loop voltage drops rapidly to zero; however, this is a less direct measurement, as an accuracy better than a few mV would be needed as will be shown later. The line-averaged density increases owing to the increased power, even though the gas valves are turned off, and then remains constant at $10^{19}m^{-3}$. The plasma elongation decreases as a consequence of profile peaking, while shaping coil currents are fixed, as κ-feedback was not active during these experiments. This shows that the equilibrium current profile relaxes to the new driven current profile within 400-500ms, with a characteristic current redistribution time $\tau_{crt} \approx 150$ms. We also show in Fig. 7 that there is no MHD activity in this fully non-inductive scenario at 124kA. The averaged efficiency, calculated using the line-averaged density, is 0.007 and corresponds to that calculated by Toray, which gives 80 ± 30kA using the error bar on T_e, n_e, and Z_{eff}, and taking into account the bootstrap current ($\approx15\%$, i.e. ≈20kA). The confinement time is about 2.1ms, 50% above scaling laws matching previous ECH scenarios in TCV. Therefore we have obtained a steady state scenario in the sense that it lasts for more than 900 confiment times and more than 10 current redistribution times.

We show in Fig. 8 that a very accurate setting of the demand current is required to obtain a true full current replacement having a flat I_{OH}. The shot 16099, I_p=124kA, is compared with two similar shots having different I_p settings: 16097, I_p=114kA, and 16098, I_p=128kA, respectively. First one sees that when I_p is smaller than the non-inductive driven current, 124kA, the ohmic transformer is recharging at a steady rate. On the other hand, in the other case the driven current is not sufficient and I_{OH} is still discharging. The shot 16098 actually disrupted near the end of the discharge because the lauching antenna mirrors moved as a result of a programming error in timing and the accidental new configuration led to a more peaked profile. In the 16098 case, the density was not exactly matched and leads to a 10% decrease in I_{CD} therefore to an effective mismatch of about 15kA. The average loop voltage for these two cases is 0.02V and -0.021V respectively, yielding a rough estimate of about 0.607kA/mV. To better characterize this ratio we show in Fig. 9 all the different averaged loop voltages obtained in these types of scenarios with 1.5MW distributed CO-CD and different settings for the plasma current, normalized to a line-averaged density of $10^{19}m^{-3}$. From the following relation: $n_{e19}I_p = c\, n_{e19}V_s + n_{e19}I_{CD} + n_{e19}I_{BS}$, where n_{e19} is introduced to annihilate the density dependence of I_{CD}, we see that the slope in Fig. 9 gives the constant c, the inverse of the plasma resistance. Note that here we compare only CO-CD cases in steady state phases and with very low loop voltage, either recharging or discharging the ohmic transformer; therefore, we are on the right-hand side of Fig. 4 in a region where the linear relationship between current and loop voltage is meaningful. Figure 9 also shows the reproducibility of our steadystate scenarios. We obtain 0.64kA/mV, which will be used in the next Section to determine the amount of current driven by the outermost-aiming gyrotron.

As a final demonstration of the accurate control of the current driven by our ECCD system and of the full sustainment of the scenario by ECW only, we show in Fig. 10 two cases with the I_p feedback turned off. The first case is an ohmic case. When the feedback control is turned off, at 0.8s, the current start to decrease while the elongation increases and the discharge disrupts owing to vertical instability.and loss of control. However in the second case, where ECCD is active between 0.4s and 2.4s as in the previous full replacement cases, the discharge continues without interruption until the power is switched off. First, one sees that there are hardly any changes when the feedback is turned off, confirming that the discharge was already fully rf-sustained at that time. One also sees that both the density and the loop voltage or I_{OH} fluctuate. This is due to an auto-feedback mechanism. We have found that in these limiter discharges the density increases when the plasma current is increased. However this in turn decreases the ECCD driven current, which then leads to a decrease in density, and so on. This is occurring between 0.8s and about 1.5s. Then, because I_{OH} is relatively high and only the voltage V_{OH} is actually kept fixed, the coils heat up leading to an increased resistivity and to a drop in current. This is why the plasma current is increasing near the end of the discharge, even though the density is also increasing. In future experiments, we will need to modify the start of the discharge such that I_{OH} can be set to zero when the ECCD is turned on.

6. Off-axis driven current

An important question is whether the outermost-aiming gyrotron, 'C' in Fig. 6a, is driving any significant current. Toray calculations indicate that only 2-5kA is expected to be driven at $\rho \approx 0.55$. Therefore this gyrotron seems useful only in broadening the pressure profile, but not the current profile. To accurately quantify the amount of current driven off-axis, we have used two methods based on comparing a discharge with all the gyrotrons providing CO-CD with a discharge where the outermost-aiming beam is turned into ECH position, in such a way as to be absorbed at the same location as during CO-CD configuration. First we compare these two discharges when the I_p current is held constant at 124kA (Fig. 11). One clearly sees that in shot 16151 with all gyrotrons in CO-CD, the 124kA current is fully replaced. However in shot 16150, with the gyrotron 'C' in heating position, the ohmic transformer is clearly discharging, indicating insufficient non-inductive current. The difference in the average loop voltage is about 11mV, which gives 7kA with the formula for the plasma conductance calculated in the previous Section. The second method consists of modifying the demand current to obtain full replacement: that is, constant I_{OH}. This is more accurate in three ways: 1) the slope of I_{OH} is a very sensitive measure of the departure from full replacement, as already mentioned; 2) only the measurement of the plasma current is needed, which is very accurate; and 3) steady state conditions with no residual electric field are used, avoiding potential modification of the current drive efficiency, albeit very small in these cases as the loop voltage is already very small. For the full CO-CD discharge, we set I_p to 117kA, due to a higher density than in previous discharges, and the ohmic transformer was slightly recharging. For the 2 CO-CD, 1 ECH case, we set I_p to 111kA, and matched the density to the previous case. Here the ohmic transformer current was constant. Therefore, there is more than a 6kA difference, that is about 7.8 ± 0.8kA of current driven at the outermost location, at $\rho \approx 0.55$. This value is somewhat larger than expected from Toray, although the difference is not very large. Note also that, even though the absolute value is small because of the low local T_e, this good current drive efficiency is encouraging for reactor-like experiments, which need very off-axis ECCD to stabilize neoclassical tearing modes [11]. The local temperature is 1 ± 0.3keV, that is about one third of the central temperature. Therefore if one assumes a constant local current drive efficiency, normalized to the local temperature and density, the beam aiming at $\rho \approx 0.4$ would drive about 12kA of current, and the central beam about 24kA for a total of about 44kA of driven current. This is much smaller than the actual driven current, ≈ 105kA, indicating that the local current drive efficiency is not constant and does suffer from the loss in efficiency owing to trapped particles, contrary to the results of DIII-D [12]. Note that in our case the collisionality ν_{e*} is small, about 0.02, and could explain this discrepancy as higher collisionality can reduced the trapped particle fraction.

7. Conclusions

We have shown that high-energy fast electron tails with characteristic photon temperatures of up to 50keV are generated in CO- and CNT-CD scenarios, but not in ECH cases. Based on the intensity of hard-X ray emission, the optimum angle for CO-CD is about 35°. Using this toroidal angle, we have obtained current drive efficiencies up to 0.016×10^{20} AW^{-1}m^{-2} with full replacement of 153kA, at $n_{e0} \approx 1.75 \times 10^{19}$m^{-3} and $T_{e0} \approx 4$keV. However these are obtained with the three 0.5MW gyrotrons aiming at the center of the plasma, leading to overly peaked pressure and current profiles. These profiles are MHD unstable and the discharge disrupts within 150ms, i.e. in the time scale of profile redistribution. Thanks to the flexibility of the TCV ECW system, we are able to distribute the beams over the minor radius in order to sustain broader profiles. In this way steady-state fully non-inductive scenarios have been obtained where 123kA of current, including 15% of bootstrap current, is fully ECCD driven for 1.9s: that is, more than 900 confinement times and more than 10 current redistribution times. The efficiency is lower as the temperature is lower in the center ($T_{e0} \approx 3.5$keV) and even lower off-axis: we obtain $\eta_{20} \approx 0.007$ with $\bar{n}_e \approx 10^{19}$m^{-3}. Note that Z_{eff} is relatively large in these low density discharges, $Z_{eff} \approx 5.4$. The total current driven is consistent with Toray calculations, within the error bars of T_e, n_e, and Z_{eff}. We have also shown that a small change in the demand plasma current can lead to steady recharging or discharging of the ohmic transformer. This is why the time evolution of the current in the ohmic transformer coils is a very sensitive measure

of full current replacement and should be used in complement to the loop voltage measurements.

We have also shown that the outermost-aiming beam, absorbed at $\rho \approx 0.55$, is driving 7.8±0.8kA, somewhat larger than the 2-5kA expected from Toray. The modest value of this current, for a 0.5MW gyrotron, is consistent with the good current drive efficiency because the local temperature is low, $\approx 1\pm 0.3keV$, Z_{eff} is large. We have shown that the current driven at the outermost location can be measured by two accurate methods, when steady-state conditions are possible. Our results indicate that the local current drive efficiency is not constant across the minor radius, but decreases due to trapping effect.

Acknowledgements

References

[1] F. Hofmann et al, *Variable Configuration Plasmas in TCV Plasma* Phys. Control. Fusion **39** (1994) Vol. 1 627-632

[2] A. Pochelon et al, *Energy confinement and MHD activity in shaped TCV plasmas with localised electron cyclotron heating*, 17th IAEA Fusion Energy Conf., Yokohama, (1998), to appear.

[3] T. P. Goodman et al, *Design and Installation of the Electron Czclotron Wave System for the TCV tokamak*, Proc. 19th SOFT, Lisbon Vol. 1 (1996) 565-568.

[4] T. P. Goodman et al, *Poloidally Asymmetric Plasma Response during ECH Experiments in TCV*, Proc. of 26th EPS conf. On Contr. Fusion and Plasma Physics, Maastricht (1999), to appear.

[5] M. A. Henderson et al., *Recent Results in ECH and ECCD Experiments in the TCV Tokamak*, Strong Microwaves in Plasmas, (1999) to appear.

[6] N. J. Fisch, *Theory of Current Drive in Plasmas,* Rev. Mod. Phys. **59**, (1987) 175-234

[7] R. A. Pitts, R. Chavan, J.-M. Moret, *The Design of Central Column Protection Tiles for the TCV Tokamak*, Nucl. Fusion **39** (1999) to appear.

[8] Y. Peysson and R. Arslanbekov, *Measurement of the Non-Thermal Bremsstrahlung Emission between 30 and 200 keV with a High Time-Space Resolution on the Tokamak TORE SUPRA*, Nucl. Instr. and Methods, 380 (1996) 423-426.

[9] S. Coda et al, *Measurements of Hard X-ray Emission Profiles in the TCV Tokamak during Electron Cyclotron Heating and Current Drive*, Proc. of 26th EPS conf. On Contr. Fusion and Plasma Physics, Maastricht, (1999), to appear.

[10] F. M. A. Smits, *Elliptical Polarization for Oblique EC-Wave Launch*, Proc. of 8th Joint Workshop on ECE and ECRH (EC-8), Gut Ising, (1993), 549-559.

[11] O. Sauter et al, *Beta Limits in Long-Pulse Tokamak discharges*, Phys. Plasmas **4** (1997) 1654.

[12] T. Luce et al, *Generation of Localized Non-Inductive Current by Electron Cyclotron Waves on the DIII-D Tokamak*, General Atomics report, (1999) GA-A23018.
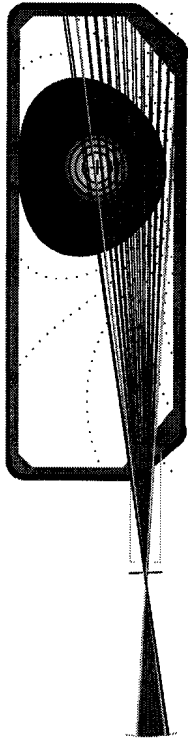
Fig. 1: Plasma cross-section showing viewing chords of the hard X-ray camera as implemented on TCV.
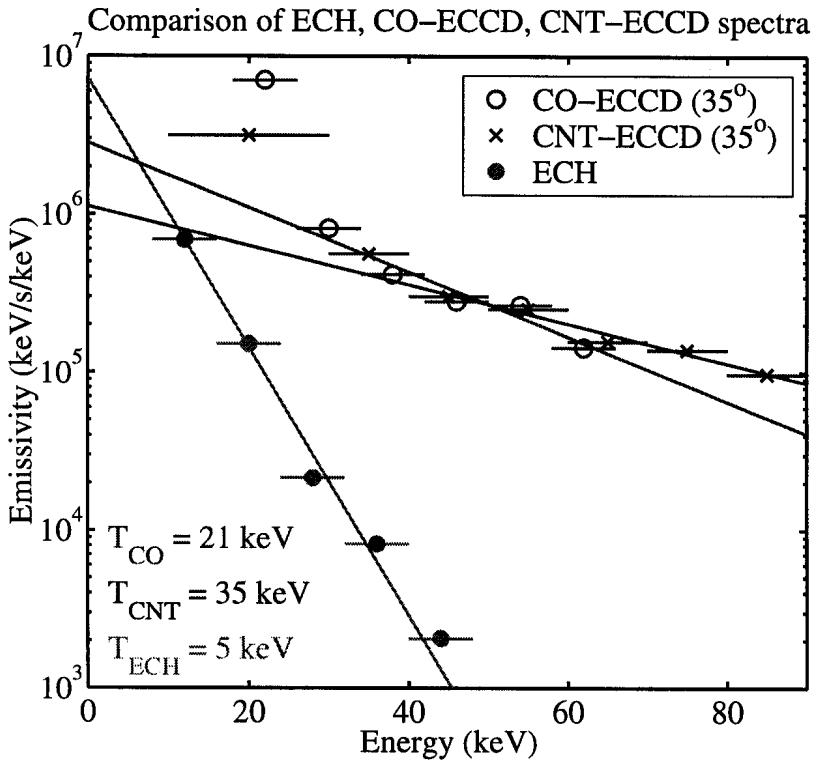

Comparison of ECH, CO–ECCD, CNT–ECCD spectra

$T_{CO} = 21\ keV$

$T_{CNT} = 35\ keV$

$T_{ECH} = 5\ keV$

Fig 2: Central hard X-ray emissivity for similar shots with CO-CD ($\varphi=35°$), CNT-CD ($\varphi=-35°$) and ECH, respectively, using 1.5MW.
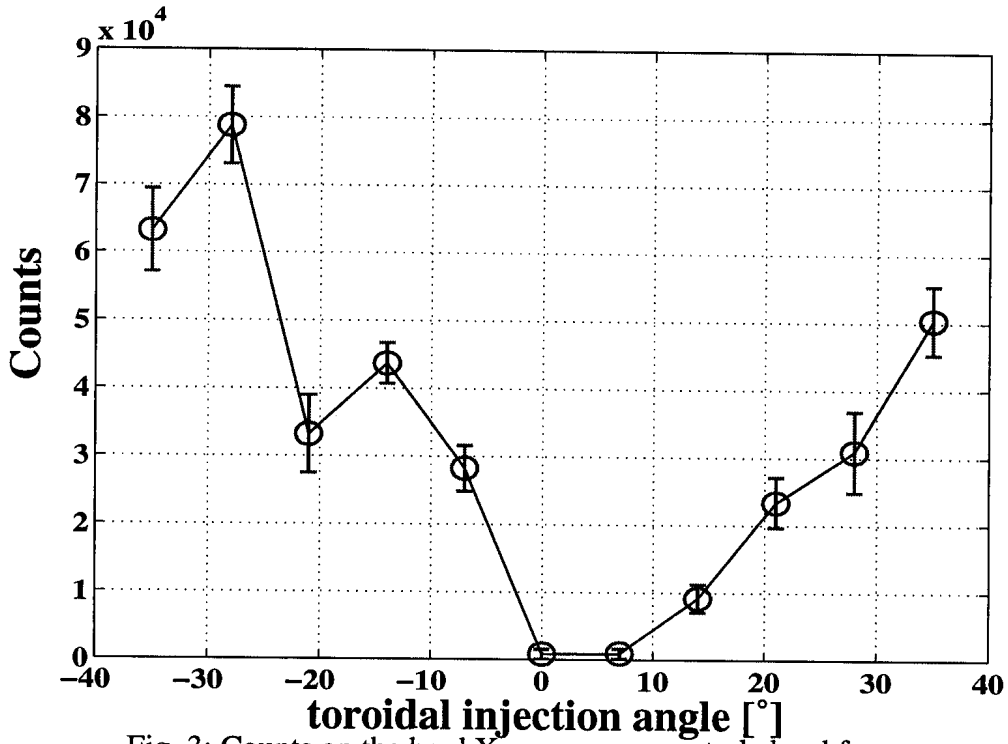
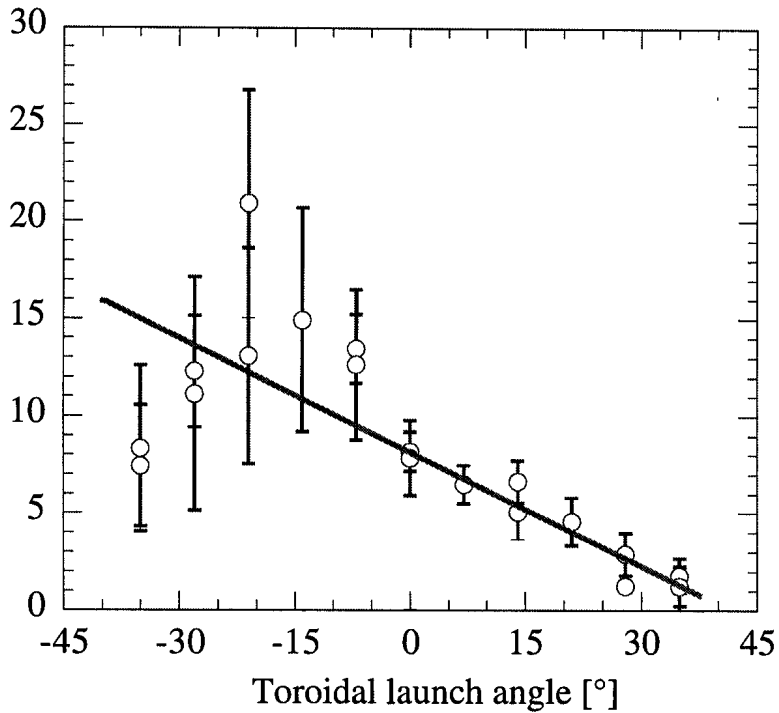Fig. 3: Counts on the hard X-ray camera central chord for $40keV<E<50keV$ as a function of the toroidal launch angle.

Fig. 4: Surface loop votage multiplied by the ratio $Te_0^{3/2}$ to account for the change in plasma resistivity and the differences in heating between CO- and CNT-CD cases for on-axis aiming.
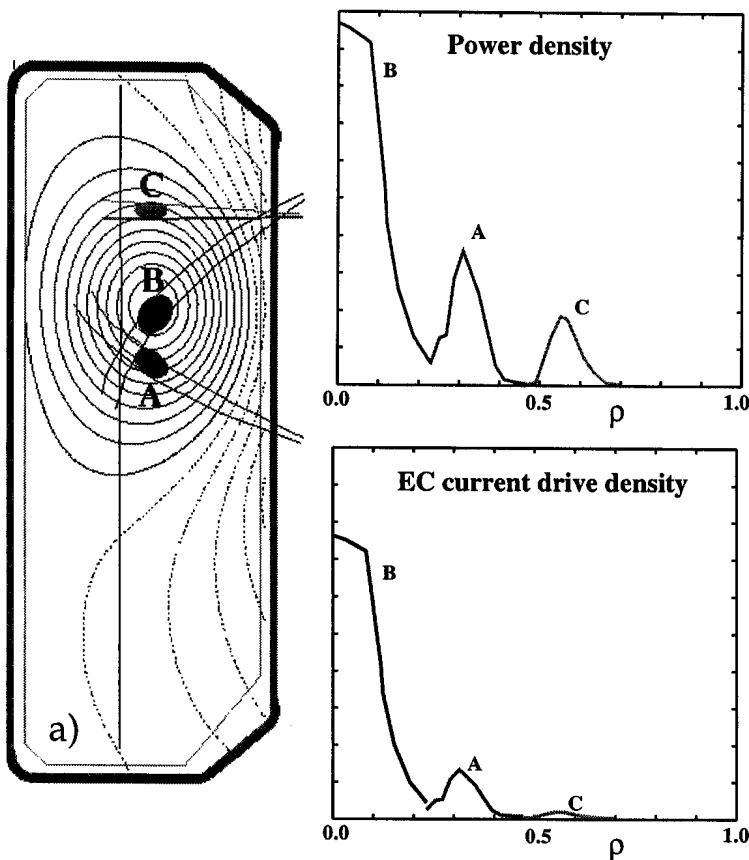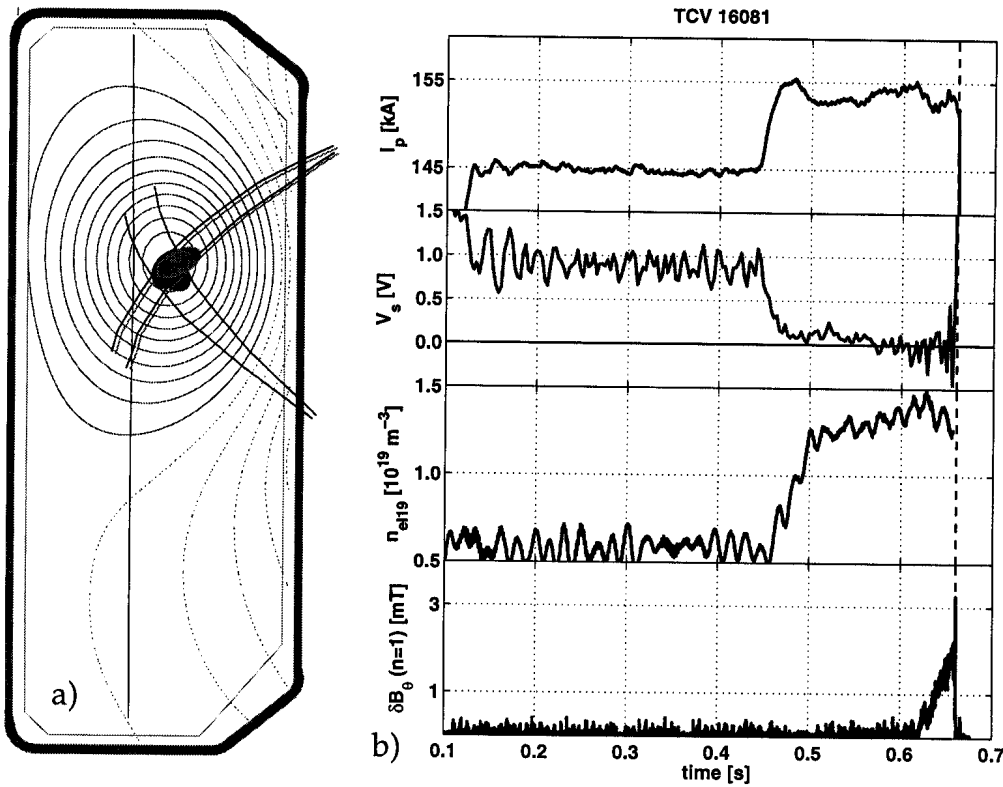
Fig. 5: (a) Beam paths for the three gyrotrons aiming at the plasma center with the localization of their absorption sketched according to Toray calculations. (b) Time traces of a discharge using the layout as in (a), with full current replacement of 153kA and disruption after about 150ms, due to too peaked profiles.

Fig. 6: (a) Beam paths and absorption spots as calculated by Toray for distributed power depostion cases. (b) Power deposition profile and local current driven as obtained by Toray for the shot 16099.

shot 16099
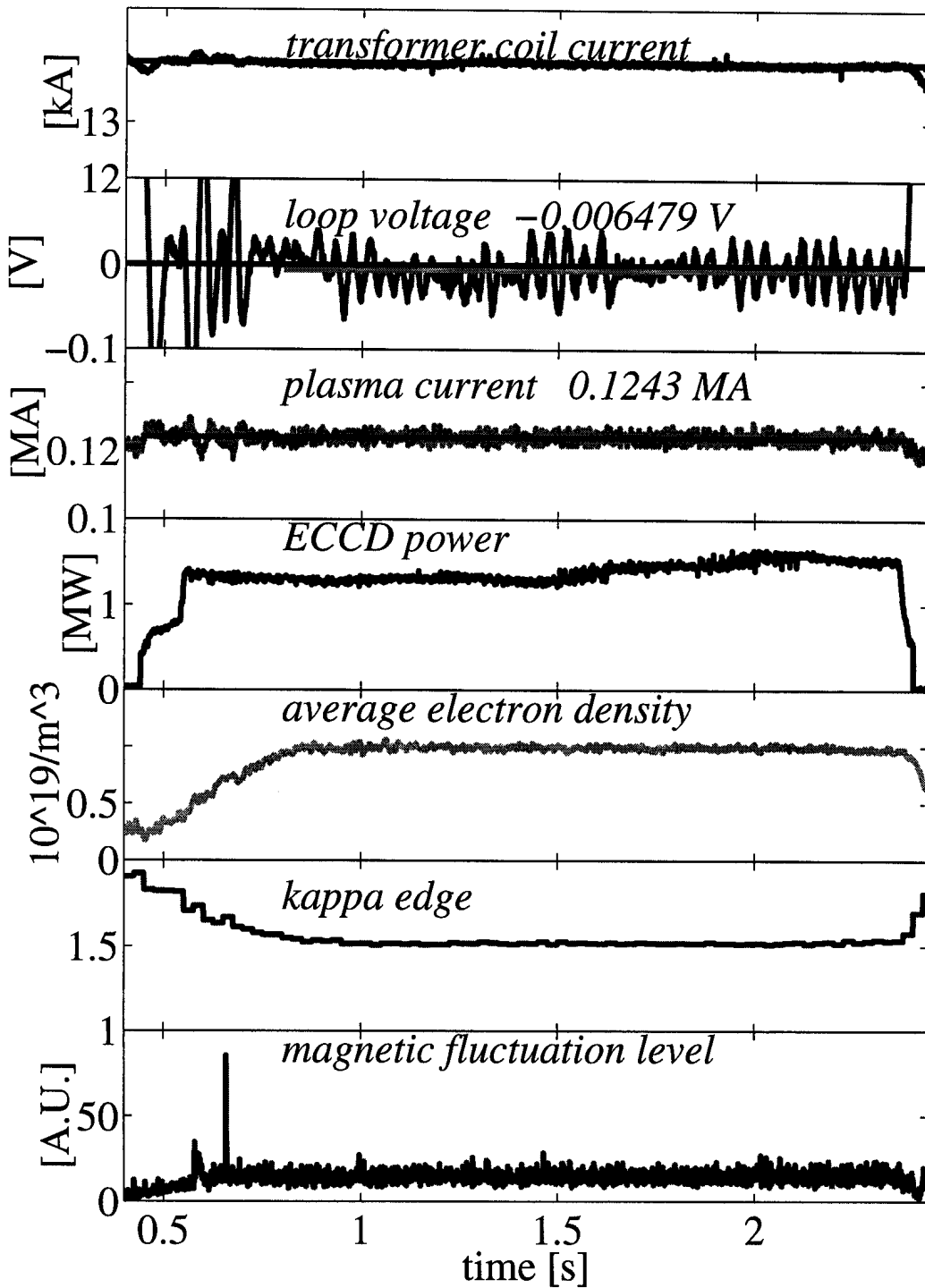
Fig. 7: Time traces of a discharge using the layout shown in Fig. 6. Steady-state full current replacement is obtained for 1.9s at 124kA, $n_e=10^{19}m^{-3}$, $T_{e0}\approx3.5keV$.
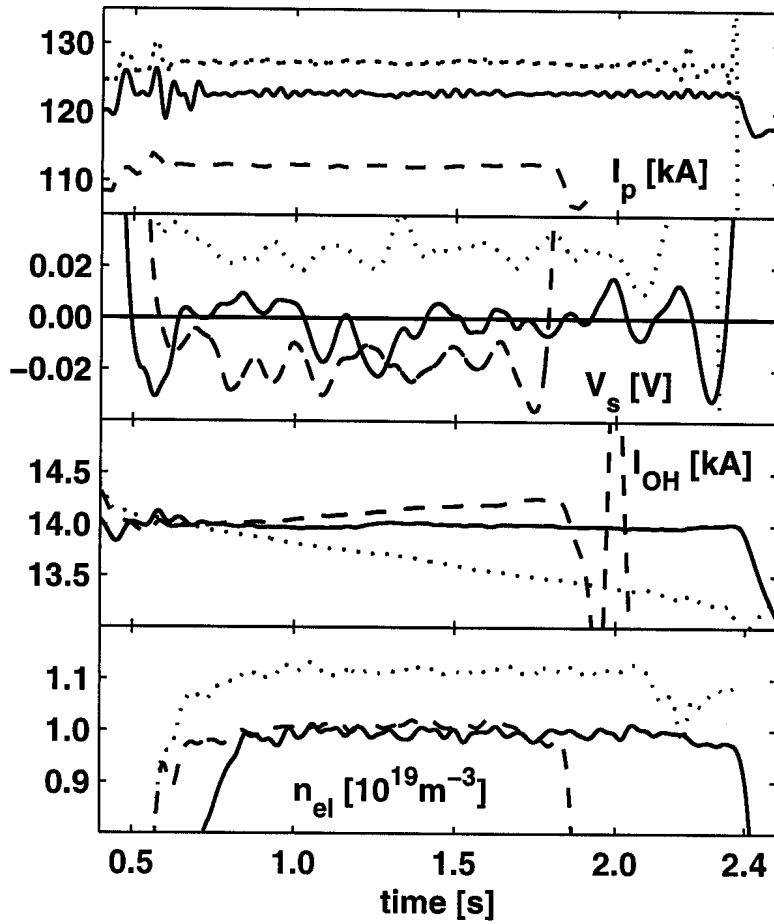
Fig. 8: Comparison of shot 16099, solid line shown also in Fig. 7, with two similar discharges having Ip=113kA (shot 16097, dashed line), and Ip=128kA (shot 16098, dotted line), respectively.

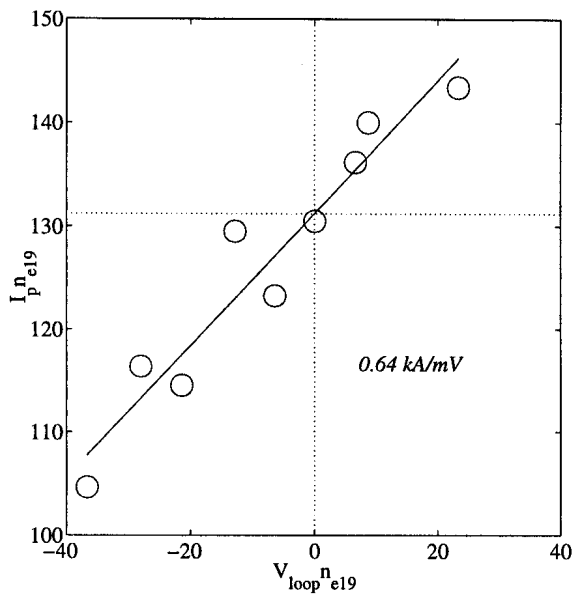Fig. 9: Plasma current vs averaged loop voltage in steady-state scenarios similar to the ones shown in Fig. 8, changing only Ip. The effect of density is taken into account.
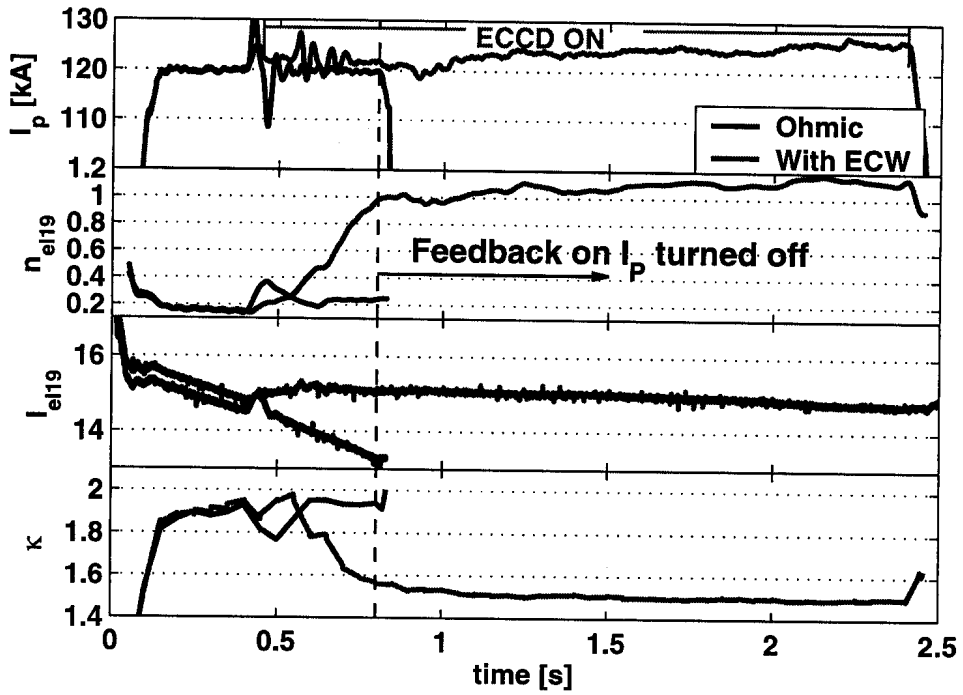
Fig. 10: Two discharges, 16152 and 16153, where the feedback on Ip is turned off at 0.8s. In the ohmic case, the current drops and the discharge disrupts, whereas in the ECCD case, the discharge continues with minimal perturbation indicating that at 0.8s the profiles and total plasma current are already fully sustained by the ECCD
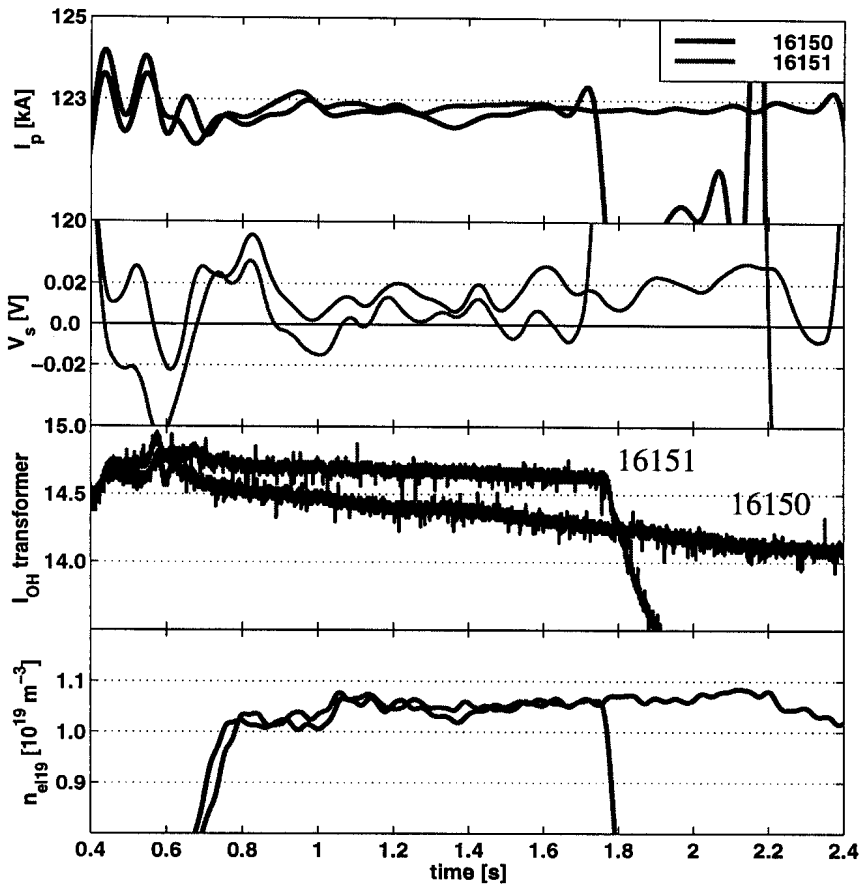

Fig. 11: Comparison of a discharge, 16151, similar to the one shown in Fig. 7, with one having the most off-axis gyrotron turned to $\varphi = 0°$, shot 16150. The densities match but the second clearly does not drive as much current than the first case.

Poloidally Asymmetric Plasma Response with ECH Deposition near q=1 in TCV

M.A. Henderson, T.P.Goodman J.-Ph. Hogge, Z.A. Pietrzyk, A. Pochelon,
O. Sauter

Centre de Recherches en Physique des Plasmas, Ecole Polytechnique Fédérale de Lausanne, Association EURATOM-Confédération Suisse, CH-1015 Lausanne EPFL, Switzerland

A small component of ECCD exists when heating off-axis with no toroidal injection due to the field helicity. The sign of the ECCD will change depending on the absorption location in a poloidal plane, the beam injection, and the direction of the toroidal magnetic field. The importance of the ECCD component can be confirmed by the behavior of the sawteeth when the ECH deposition crosses the q=1 surface. Sawtooth period is very sensitive to the local shear at q=1 and it is shown that difference in sawtooth period when heating above and below midplane are consistent with the presence of a small ECCD component. Experiments have also shown that the sawtooth period is strongly determined by the absorbed ECH power density near the q=1 surface. In particular significant changes in the sawtooth period are observed as the absorption location is varied on a scale smaller than the beam spot size. An energy barrier associated with the q=1 surface is shown to be located outside the q=1 surface by a factor of 1.3 in radii. The barrier can be used as a method for measuring the beam deposition width in the plasma.

1. Introduction

A unique advantage of an ECH system is the possibility to direct the beam and deposit the power locally in the plasma discharge. The size of the ECH deposition is small relative to the plasma size and this can be used to modify current and pressure profile, sawtooth stability, etc. The ECH system on TCV is designed to allow the beam to be deposited across a large portion of the vessel cross-section and investigate such local deposition effects. During sweeps of the beam in a poloidal cross section of the plasma large sawteeth with an increased period were observed near the q=1 surface. The large sawteeth occur over a smaller region than the beam width [1]. This report investigates the dependencies of the sawtooth behavior on the power density and ECCD component on the q=1 surface.

Previously, experiments on TCV have shown a change in the confinement between inside and outside q=1 deposition [2]. This effect maybe due to an energy transport barrier which is shown here to be small in width and located outside of the q=1 surface. It is possible that this barrier is the mixing radius associated with the q=1 resonant flux surface [3].

2. Experimental setup

The TCV-ECH system [4] when complete will consist of nine gyrotrons of 0.5 MW each. Six gyrotrons will operate at the second harmonic frequency (X2) of 82.7 GHz and three at the third harmonic frequency (X3) of 118 GHz. ECH experiments on TCV have operated with 1.5MW, 2.0s delivered to TCV. In this report three X2 gyrotrons are used but with a total delivered power of only 1.0 MW. Each X2 gyrotron is connected to a matching optics unit (MOU) for coupling into the evacuated corrugated waveguide and absorption of stray radiation from the gyrotron. Incorporated in the MOU is a Universal Polarizer providing the full range of all possible polarizations for optimum coupling in ECH and ECCD scenarios on TCV. Connected to each MOU is an evacuated transmission line (approximately 30 m of 63.5 mm corrugated HE_{11} waveguide) and a launching antenna (launcher).

The X2 launcher is designed to direct the microwave beam at any radial location within the wide range of plasma shapes achievable on the TCV tokamak. Currently, there is one launcher (L1) mounted in an equatorial port and two launchers (L2 and L3) mounted in upper lateral ports (see

Fig. 1). Each launcher has 2 degrees of freedom, the first provides steering of the beam in a fixed plane during a shot, realized by rotating the last mirror (55° in 300 ms). The second degree of freedom allows that plane to be rotated about the axis of the launcher port between shots to introduce a toroidal injection angle (-180° to 180°). Each gyrotron can be independently switched to the torus or to a calorimetric load from shot to shot, such that power can be delivered from any possible combination of three launchers for a given shot (three gyrotrons form one cluster which are powered from one single Regulated High Voltage Power Supply).

The soft X-ray diagnostic provides the most direct response of the central MHD activity and is currently comprised of two groups of instruments. The first consists of four vertically viewing, fast diodes with a sampling rate of 250 kHz located in four toroidal positions provide high time resolution of MHD activity. The
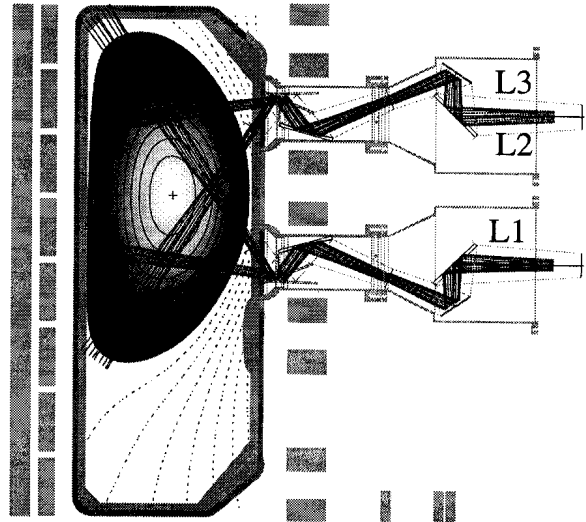

Fig. 1. Poloidal view of X2 launcher accessibility is shown. Currently three launchers are installed on the torus, one in a equatorial port (L1) and two in upper-lateral ports (L2 and L3).

second, 180 diodes distributed in nine cameras in one poloidal cross section with sampling rate of up to 80 kHz and spatial resolution of 3.5 cm after tomographic reconstruction.

The Thomson scattering system [2] on TCV uses three Nd:YAG lasers (each at 20 Hz, combined in a fan and focused to a single point in the plasma) aligned in the vertical direction at a common value of the major radius. Thirty-five viewing chords are distributed on three horizontal ports providing a measure of n_e and T_e with a typical spatial resolution of about 4 cm along the laser beam.

The LIUQE equilibrium code [5] determines the plasma position and shape from 38 magnetic probes and the plasma pressure profiles from the Thomson scattering system. These results along with the Thomson density and temperature profiles are used by the TORAY [6,7] ray tracing code to compute the beam propagation and absorption location, as well as the amount of current driven and the fraction of single-pass absorption from the injected ECH beam.

3. Results

Initial ECH experiments on TCV included the sweep of the beam across a vertical chord of the plasma. The beam is launched in X-mode during the sweep; the calculated absorbed power is 100% and the coupling changes by less than 5% during the sweep of the beam. The plasma (n_e=1.4-1.9x10^{19} m^{-3}, I_p=193 kA, κ=1.3, δ=0.3) response to the sweep exhibits an increase in T_e and soft X-ray signals when deposition was inside the q=1 surface. Large sawteeth are observed when the beam deposition is on the q=1 surface closest to the launcher. These sawteeth occur over a relatively small region (~10 mm) during the sweep compared to the beam width (~25mm). The location of the q=1 surface, which is assumed to be equal to the inversion radius of the soft x-ray signal and modeled via LIUQE, corresponds to the deposition location for the large sawteeth. However, the inversion radius is obtained from the soft X-ray tomography with a pixel spacing of ~3.5 cm. LIUQE results calculate the q=1 surface with an accuracy of ~3 cm. The resolution of both the inversion radius and the LIUQE calculated q=1 surface are insufficient in confirming the peak of the sawtooth period as the location of the q=1 surface. Note that the peak of the sawtooth period is well defined, consistent within ±2mm [1] for this target plasma over several shots spanning three campaign periods. The localization of this effect is extremely sensitive and should provide a more accurate measure of the q=1 rational surface than other existing techniques. This report will refer to the location of the peak in the sawtooth period as the "q=1" surface, at ρ =ρ_1, with the quotations emphasizing the uncertainty of the exact location of the true q=1 rational surface. Unfortunately, existing diagnostics of the q=1 surface are not able to measure its location

within the required accuracy obtained in locating the peak in the sawtooth period and therefore, are unable to confirm this supposition. The locations of the large sawteeth have been used to insure similar alignment of the three separate launcher systems to within ±3mm [8].

Comparing the plasma response for two launchers located at different vertical heights reveal an asymmetry when heating symmetrically above or below the midplane. This asymmetry is best observed in comparing the sawtooth shape and period when the deposition is on the "q=1" surface above and below the midplane using the upper lateral (L3) and equatorial (L1) launchers respectively (see Fig. 2). Above the mid-plane the sawteeth are large triangular with a period of ~8ms relative to ~1-2ms during ohmic and ECH (non "q=1" deposition) phases. Below the midplane the sawteeth are humpback-like and a peak period of ~5ms, see Fig. 3. Even though the sweep of the beam was kept in a poloidal plane (no toroidal injection angle), the asymmetry has been shown to be a result of the small current drive component. The ECCD component arises from the non-zero projection of the wave vector **k** on the magnetic field for off-axis heating - thereby producing Doppler-shifted absorption [9], see Fig. 4. The large triangular sawteeth occurring with a co-ECCD component (deposition on top) and the humpback-like sawteeth with a counter-ECCD component (deposition on bottom). The direction (co/counter) and magnitude of ECCD will depend on the absorption location, launch direction (HFS versus LFS) and toroidal field direction but not on the plasma current direction. Because it is the poloidal field that creates the asymmetry, the effects are seen only during off-axis absorption. The off-axis co- and counter-ECCD component is confirmed by TORAY calculations that show linear current drive efficiencies changing sign when heating above or below the plasma midplane, albeit of small amplitude (~5kA). The small amplitude is, in fact, significant since the change in the sawtooth behavior occurs with only 5kA in a plasma discharge of 193kA.

Following the above argument, the direction of the ECCD component should be reversed (thus flipping the role of the two launchers in the asymmetry of the sawtooth shape and period) when reversing B_ϕ. With B_ϕ positive the large triangular sawteeth with large period are observed above the midplane,

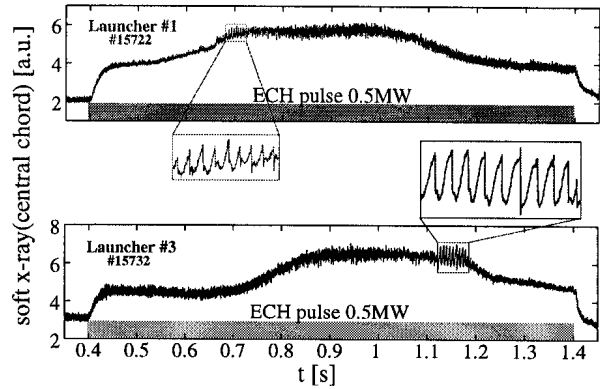

Fig. 2. Evidence of the up-down asymmetry as seen from the sawtooth shape when heating on the bottom (Launcher #1) or top (Launcher #3) q=1 surface. Large triangular sawteeth with increased period occur when heating on top versus humpback-like when on bottom. Power and power density at the large sawteeth are the same for the two sweeps.
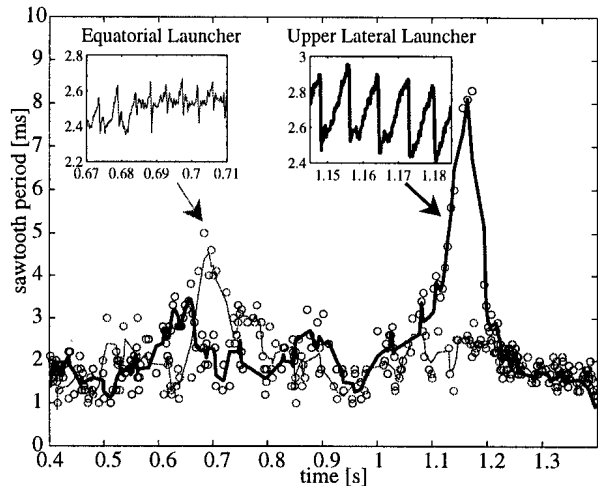

Fig. 3. Asymmetric response to the Sawtooth period as the beam is swept through the q=1 surface. Sawtooth period increases when deposition is on the "q=1" surface with maximum period when on top [9].
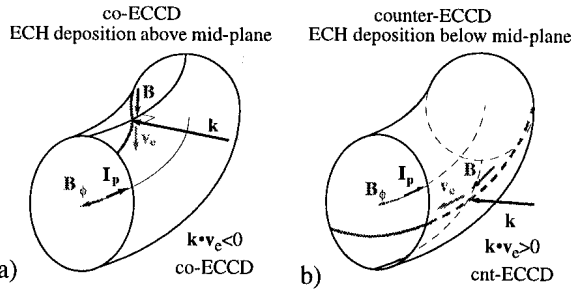
with B_ϕ negative these sawteeth are observed below the midplane. During the flipping of B_ϕ all other parameters were kept relatively constant. This implies the sawtooth shape and period are dependent upon the polarity of the driven current on the "q=1" surface, with the co-ECCD component increasing the sawtooth period [9].

co-ECCD
ECH deposition above mid-plane

counter-ECCD
ECH deposition below mid-plane

Fig. 4. Asymmetry is due to an ECCD component arising from a poloidal component of **k** along the electron trajectory. With B_ϕ defined as shown the ECCD component is co- when heating above the axis and counter- when heating below [8]

This hypothesis is further tested by performing similar sweeps of ECH deposition across the "q=1" surface and introducing a non-zero toroidal angle (at the launcher) to enhance or eliminate the ECCD component at the deposition location. The peak sawtooth period, as the beam is swept across the "q=1" surface, increases linearly with local toroidal angle at the resonance surface, see Fig. 5. The local toroidal angle at the field line is shown to be 0° (pure ECH) when introducing an -8° toroidal rotation of the launcher. In the case of no toroidal injection at the launcher, the local toroidal angle at the resonance is of the order of ~5°. TORAY calculates the associated co-driven current as 5kA (0.01A/W) with a plasma current of 193kA. The magnitude of the driven current is dependent on the local rotational transform, the electron temperature at the deposition, the deposition location and the injected beam angle. The difference in the local toroidal angle for off-axis deposition between above and below the midplane deposition is ~10° during nominally ECH conditions (for $q_{edge} \approx 4$). This difference between top and bottom depositions corresponds to +/- 5kA which is significant when optimizing for off-axis ECCD [10] and should be taken into account when designing an ECH system for optimizing off-axis ECCD.
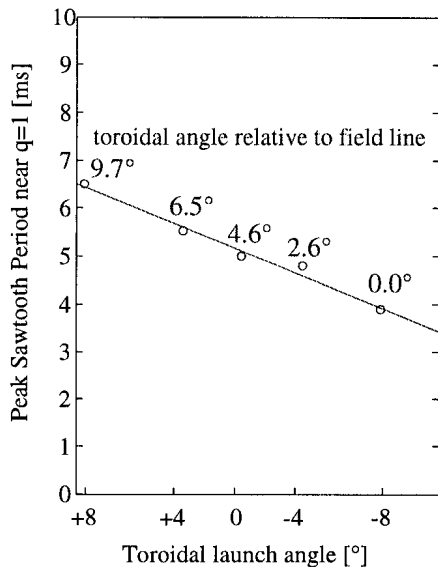
Note that the polarity of the off-axis ECCD component is determined by the direction of B_ϕ, deposition location and injected beam angle.

Scans of the power density on the "q=1" surface are performed with constant deposition profile. The ECH power is ramped from 0.2 to 0.5 MW with a single beam fixed on the top "q=1" surface nearest the chosen launcher, see Fig. 6. The power ramp is repeated with the addition of a second beam increasing the total power from 0.4 to 1.0 MW. During the two scans the sawtooth period increases linearly with the deposited ECH power on the "q=1" surface.

A third scan was performed with two beams positioned symmetrically just inside and outside of the location of the "q=1" surface. The two beams are swept in time across the "q=1" position. During the sweep the beams are kept at constant power so that the total power inside the "q=1" is kept constant and only the local power intensity on the "q=1" changes during the sweep. As the beams approach the "q=1" surface the sawtooth period increases, with a maximum when the two beams coincide. As the beams pass over the "q=1" surface the sawtooth period decreases. Since the power inside and outside the "q=1" was constant, the change in the sawtooth period is attributed to the change in the local power intensity on the "q=1" surface. The sawtooth period varied linearly with the local power on the "q=1" surface as with the power scans described above. All three of the previous described scans were performed with equivalent co-ECCD component calculated from TORAY.

Fig. 5. Sawtooth period increases as the toroidal component on the "q=1" surface increases. The toroidal launch angle is introduced at the launcher, which changes the local toroidal angle at the deposition. For nominal ECH (no toroidal injection angle) there is a ~5° toroidal angle. The sawtooth period increases with the co-ECCD component on the q=1 surface.

High power density on the "q=1" surface can also be obtained when depositing the ECH power on the HFS and varying B_ϕ so that the deposition sweeps across the "q=1" surface along

the major radius. Even though a single beam is used the power density in normalized radius ρ is of the order of the 1.0MW two beam scans above. Including this sweep with the above power scans show a linear dependence on the sawtooth period with the local power density (within the investigated range), see Fig. 6.

The sawtooth period's dependence on the local power density can be used as a tool for determining the beam deposition within the plasma [9]. As has been shown, the sawtooth period responds to the local power density on the "q=1" surface. Sweeping the beam slowly across the "q=1" surface at a constant rate, the sawtooth period follows a Gaussian profile. Fitting the sawtooth period to a gaussian yields the width of the power deposition in the plasma, width ~24mm, and is comparable to TORAY results for the power deposition in the plasma. The free space beam waist at this location is calculated to be ~25mm.

Sweeps of the ECH deposition identical to those described above were performed with non-optimal coupling of the beam by changing the X-O mode fraction via the Universal Polarizer located in the MOU. The soft X-ray signal viewed from a central chord increases when the deposition is inside the "q=1" surface for X-mode launch. This rise is barely apparent for the O-mode injection. For X-mode launch the total electron energy from Thomson scattering shows a ~23% increase when the ECH deposition enters into the q=1 region for these discharges. O-mode launch between deposition inside and outside the "q=1" surface increases the total power by only ~4%, see Fig. 7. TORAY predicts 100% absorption for X-mode while only ~12% for O-mode. For power absorbed in the plasma with random radiation (as in the case of second-pass absorption from O-mode injection) a multi-pass absorption model [8] is used to estimate an additional 53% of the injected power is absorbed in the plasma during O-mode injection. The difference in the total energy of the two sweeps and the increase in total energy with deposition inside the "q = 1" surface is attributed to an increase confinement when inside the "q=1". This suggests the presents of an energy barrier near ρ_1.

The soft X-ray emission viewed from a central chord divided by the line average density follows a similar behavior as that of the total
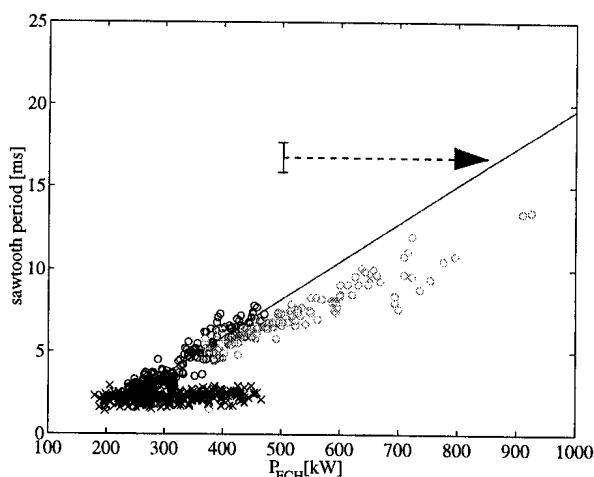

Fig. 6. Sawtooth period increases linearly with power on the q=1. Beam profile was kept constant during the sweeps so power density scales linearly with injected power. Several sweeps are included in this power ramp: x – 0.2 to 0.5 MW power ramp slightly off of the "q=1" surface, o – repeat of the power ramp on the "q=1" surface, o – 0.4 to 1.0 MW power ramp at higher density (density correction brings points up to line), arrow – b_ϕ scan corrected for the high power density in ρ.
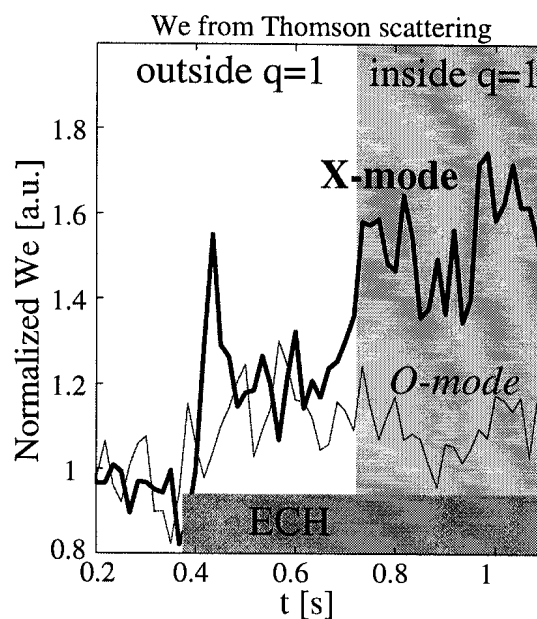

Fig. 7. Total stored energy in plasma normalized to ohmic for deposition outside and inside the "q=1" surface for X-mode (99%) and O-mode (4%) coupling. The total energy rises as the beam enters the "q=1" surface by 23% for X-mode and 4% for O-mode. Rise in the X-mode trace suggests the presence of an energy barrier near the "q=1" surface [8].

stored energy in the plasma for the O- and X-mode sweeps. The change in energy flux inside the barrier region can be obtained from the time derivative of the smoothed soft X-ray emission signal,

dI_{SX}/dt. For the X-mode launch the peak of the derivative yields the location of the energy barrier for the two transitions, see Fig. 8, and is located ~19mm outside that of the peak from the maximum of the sawtooth period. This implies that there are two separate surfaces within this region, one for the peak in the sawtooth period and a second further outside for the energy barrier, with the accuracy of determining each surface is $\leq\pm3$mm. The energy barrier is $1.3 \bullet \rho_1$ which suggests that the barrier is related to the energy mixing radius of the q=1, $\rho_{mix} \approx 1.4 \bullet \rho_1$ [3]. Gaussian fit of the derivative yields the deposition width of the beam as it enters (leaves) the barrier region assuming that the width of the barrier is small relative to the beam deposition width, see Fig. 9. Results of the fit on the near q=1 side yield similar results as obtained from the results of the sawtooth period deposition fits (~29mm versus ~24mm). Since the deposition width from dI_{SX}/dt fits well to the deposited beam, the barrier region must be small in comparison to the deposition size, << 25mm. A large barrier width would broaden the apparent beam width using this technique. The measured beam width is comparable to the beam deposition calculated from TORAY. This technique can be used for determining the beam deposition in the plasma and a comparison to the deposition profiles obtained from ECE and soft x-ray.

4. Conclusions

The sawtooth period has been shown to increase with the deposited ECH power density on or near the q=1 surface. The period is also dependent on the ECCD component of the beam when deposited on the q=1 surface: co-ECCD increases the sawtooth period and amplitude. It is shown that a small amount of ECCD, of the order of 5kA in the plasma of 193kA, is sufficient to dramatically change the sawtooth behavior. The localization of the large sawteeth occur in a small spatial region and is suggested as a more accurate measure of the q=1 location than current diagnostics and models. A transport barrier is shown to exist just outside the "q=1" surface at $\rho=1.3\bullet \rho_1$. The barrier may be mixing radius which is located at $\rho_{mix}=1.4\bullet \rho_1$. The barrier is shown to be smaller than the beam deposition size, and can also be used to determine the deposition of the beam as it is swept across the barrier region.
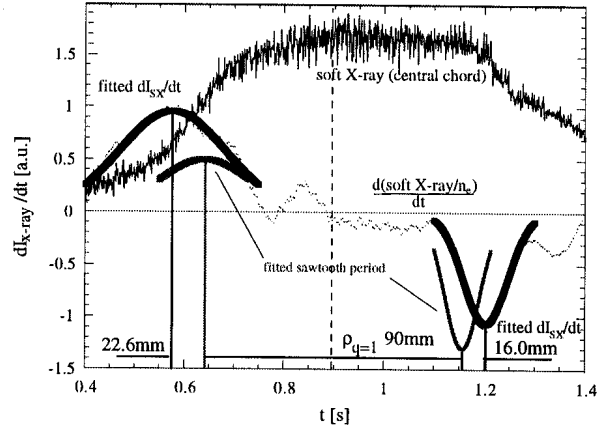

Fig. 8. Intensity of the soft x-ray signal viewed from a central chord. The derivative of the smoothed signal divided by the line average density is also shown. The peak-trough portrays in increase-decrease of energy flux into the improved confinement region. The peak represents the location of the barrier which is well outside of the location of the "q=1" surface represented by the peak in the sawtooth period.
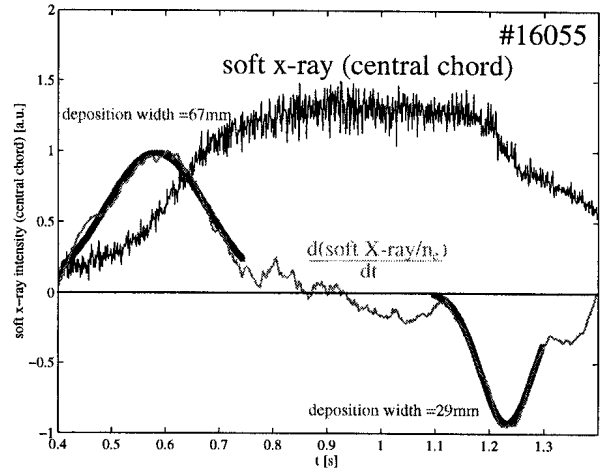

Fig. 9. The peaks from the derivative of the soft X-ray intensity divided by the line average density can be fitted to a Gaussian profile to yield the beam deposition across the barrier surface. The left fitted deposition width is larger from a stronger refraction due to a longer path through the plasma. The fitted value at the side nearest the launcher (width of 29mm) agrees well with the free space spot size at the resonance (width $\approx$25mm).

References

[1] T.P. Goodman et al., Observations in Up-Down Differences in Plasma Response during ECH on TCV, Proc. of Joint ICPP 1998 and 25th EPS Conf. On Contr. Fusion and Plasma Physics, Praha 1998, ECA **22C** (1998) 1324-1327.

[2] Z.A. Pietrzyk et al., Behavior of Central Plasma Relaxation Oscillations During Localized Electron Cyclotron Heating on the TCV Tokamak, Nuclear Fusion 39 (1999) 587-611.

[3] F. Porcelli et al., Macroscopic Magnetic Islands and Plasma Energy Transport, Phys. Rev. Lett. **62** (1999) 1458-1461.

[4] T.P. Goodman et al., Design and Installation of the Electron Cyclotron Wave System for the TCV Tokamak, Proc. 19th SOFT, Lisbon vol. 1 (1996) 565-568.

[5] F. Hofmann and G. Tonetti, Tokamak Equilibrium Reconstruction using Faraday Rotation Measurements, Nuclear Fusion **28** (1988) 1871-1875.

[6] K. Matsuda, , IEEE Trans. Plasma Sci. **17** (1989) 6.

[7] R.C. Meyer, M. Porkolab, G.R. Smith, Electron Cyclotron Wave Propagation and Absorption in the Compact Ignition Tokamak, Nuclear Fusion **29** (1989) 2155-2163.

[8] M.A. Henderson et al., Recent Results in ECH and ECCD Experiments in the TCV Tokamak, Strong Microwaves in Plasmas, (1999) to appear.

[9] T.P. Goodman et al., Poloidally Asymmetric Plasma Response during ECH Experiments in TCV, Proc. of 26th EPS Conf. On Contr. Fusion and Plasma Physics, Maastricht 1999, to appear.

[10] O. Sauter et al., Current and Pressure Profile Control using ECCD and ECH in TCV, Proc. of 26th EPS Conf. On Contr. Fusion and Plasma Physics, Maastricht 1999, to appear.